Chemical Geology 646 (2024) 121895

Contents lists available at ScienceDirect

Chemical Geology

journal homepage: www.elsevier.com/locate/chemgeo

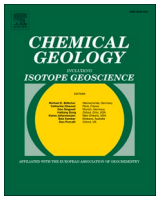

Multi-phase quantitative compositional mapping by LA-ICP-MS: Analytical approach and data reduction protocol implemented in XMapTools

Thorsten Andreas Markmann [a,*], Pierre Lanari [a], Francesca Piccoli [a], Thomas Pettke [a], Renée Tamblyn [a], Mahyra Tedeschi [b], Mona Lueder [a], Barbara E. Kunz [c], Nicolas Riel [d], Joshua Laughton [e]

[a] Institute of Geological Sciences, University of Bern, Baltzerstrasse 3, CH-3012 Bern, Switzerland
[b] Universidade Federal de Minas Gerais, Programa de Pós-Graduação em Geologia, CPMTC-IGC, Campus Pampulha, Belo Horizonte, Brazil
[c] School of Environment, Earth and Ecosystem Sciences, The Open University, Walton Hall, Milton Keynes MK7 6AA, UK
[d] Institute of Geosciences, Johannes Gutenberg-University, Mainz, Germany
[e] Department of Earth Sciences, University of Western Ontario, London, Ontario, Canada

ARTICLE INFO

Editor Name: Dr. S Aulbach

Keywords:
Laser ablation ICP-MS
Inhomogeneous materials
Major to trace element geochemical mapping
Element zoning
Petrogenesis
XMapTools

ABSTRACT

Mapping of trace element signatures is an expanding tool in geoscience and material sciences, which allows the study of solid materials, and processes that may not be captured by major elements. Developments in laser-ablation inductively-coupled-plasma mass-spectrometry (LA-ICP-MS) capabilities in the last decade now provide the necessary spatial resolution for in situ element mapping. The acquisition of two-dimensional, fully quantitative and geologically meaningful data with LA-ICP-MS is still a challenging task, and a particular obstacle is the calibration of inhomogeneous phases, such as chemically zoned minerals. This work presents a novel approach to data reduction and image generation for multi-element mapping employing LA-ICP- quadrupole MS (LA-ICP-QMS), implemented in the free and open-source software XMapTools. Three geological applications are presented to illustrate the benefits of the procedures. Garnet from an eclogitic sample (Lato Hills, Togo) and plagioclase, K-feldspar, biotite from a migmatite sample (El Oro Complex, Ecuador) were mapped multiple times at different spatial resolutions to test the calibration quality and chemical detection capabilities. Rutile in a metapelite sample (Val Malenco, Italian Alps) was mapped, and Zr-in-rutile thermometry shows a temperature range of 510 to 550 °C within a single grain. The accuracy of the LA-ICP-MS method was verified by comparison with zoned major and minor element maps (garnet, plagioclase) and Ti-in-biotite geothermometry maps obtained by electron probe microanalysis (EPMA). A spatial resolution of up to 5 μm is achieved with LA-ICP-QMS, which is similar to the resolution reported for LA-ICP time-of-flight mass spectrometry (LA-ICP-TOFMS), albeit at significantly lower acquisition speed. Maps with lower spatial resolution offer better chemical detection power as demonstrated by lower per-pixel limit of detection (LOD) map calculation. Moreover, such maps are also recorded faster. The pixel allocation strategy and the instrumental conditions also have a direct impact on map quality. We recommend that maps are interpolated to square pixels, where a pixel consists of multiple sweeps to gain an improved detection power. Benchmarks using an emulated LA-ICP-MS mapping show that the spot size, together with scan direction, can lead to a shift in composition depending on the feature size of chemical patterns. This is verified by mapping a thin 10 μm annulus in garnet visible in REE and such compositional shifts can have a significant impact on e.g., diffusion modelling. The new software solution provides a multi-standard and variable composition calibration of LA-ICP-MS maps with single pixel LOD filtering at 95% confidence, allowing the user to quantify inhomogeneous materials of major and trace elements simultaneously with improved accuracy.

* Corresponding author.
E-mail address: thorsten.markmann@unibe.ch (T.A. Markmann).

https://doi.org/10.1016/j.chemgeo.2023.121895
Received 26 October 2023; Received in revised form 14 December 2023; Accepted 15 December 2023
Available online 20 December 2023

1. Introduction

The use of laser-ablation inductively-coupled-plasma mass-spectrometry (LA-ICP-MS) mapping has increased dramatically over the past decade, especially for in situ (semi-) quantification of major, minor and trace element compositions of geological materials (Phillips et al., 2023; Raimondo et al., 2017; Rubatto et al., 2020; Ubide et al., 2015; Ulrich et al., 2009). LA-ICP-MS is commonly used for single-spot measurements where the signal is integrated over the ablation crater, which is approximately 10–30 μm deep. Spot locations can be determined using surface imaging techniques that capture the uppermost few micrometers of the sample only. The homogeneity of the sample with depth remains unknown except for transmitted light microscopy inspection for the presence of inclusions or cracks; however, the transient signal acquired in single spot mode offers information on whether sample composition is homogeneous down the ablated crater depth. An alternative strategy is to use line scanning instead of single spots to collect intensity data that can be calibrated to produce chemical maps (Paton et al., 2011; Woodhead et al., 2008, 2007). Although quantitative compositional mapping is common for other instruments such as electron probe micro-analysis (EPMA) (e.g., Lanari et al., 2019), the analytical protocol development for LA-ICP-MS mapping is much less advanced. This is due to both analytical and data reduction challenges. Developing an analytical protocol implemented in publicly available software for broader use can therefore help to advance the applicability of LA-ICP-MS mapping methods and, for example, reveal previously unseen details missed by single spot data acquisition routines.

Most LA-ICP-MS systems in geological laboratories can be used for mapping, provided an automated sample stage with μm resolution and ≤2 μm positioning accuracy is available. A simple mapping protocol can be easily implemented as it requires little sample preparation, and several analytical strategies are available (Ubide et al., 2015; Ulrich et al., 2009). The number of elements analyzed in mapping mode with a quadrupole can reach well over 30 with best detection capabilities at the sub-μg/g level within measurement times >4 h (Lanari and Piccoli, 2020; Raimondo et al., 2017). More complex techniques have also been developed to address the limitations of the approach, particularly in terms of spatial resolution. For example, custom-designed systems have been used to resolve single-pulse signals by combining ultrafast laser cells with specific data processing algorithms to achieve sub-spot resolution (Fox et al., 2017; Plotnikov et al., 2008; Van Malderen et al., 2015). This allows the study of synchronization problems between the pulsed laser ablation and the ICP-MS signal recording processes, known as aliasing, as well as artefacts such as blurring and smearing (Gundlach-Graham and Günther, 2016; Norris et al., 2021; Pettke et al., 2000; van Elteren et al., 2019). However, such analytical setups are usually limited to a more restricted number of elements and often require longer measurement times (e.g., Fox et al., 2017). Quantitative compositional mapping using laser ablation time-of-flight MS (LA-ICP-TOFMS) extends the application to higher spatial resolution, faster measurement and a larger set of elements to be measured in one experiment, albeit at higher limits of detection (LOD; Rubatto et al., 2020; Savard et al., 2023).

Regardless of the measurement protocol chosen, a software solution is required for data reduction and processing of LA-ICP-MS maps. Several software solutions exist in the geochemical community (see Chew et al., 2021, for a review). All provide basic tools for converting the raw signal into element intensity maps in *X*–*Y* space. This step requires a background correction, followed by a drift correction using the intensity of a known reference material. The maps can be calibrated using an external and internal standardization procedure, provided that an elemental composition for a single mineral can be fixed to a spatially constant value as an internal standard and the composition of the same element in a well-characterized calibration material is known as an external standard (see Table 1 for definitions). However, most natural materials like minerals show compositional zoning (e.g., Tracy, 1982) or do not have an element with a constant stoichiometry (e.g., amphiboles, phyllosilicates, feldspars, spinel), necessitating a new solution for internal calibration. After calibration, the map data can be displayed in various chemical diagrams (Lanari and Piccoli, 2020; Raimondo et al., 2017). The most popular software solution for the construction and calibration of LA-ICP-MS maps is the commercial software IOLITE (Paton et al., 2011) with the add-ons CellSpace (Paul et al., 2012) and Monocle (Petrus et al., 2017). Quantitative maps generated with IOLITE can be imported into XMapTools (Lanari et al., 2014, 2019) for further transformations and data visualization (Lanari and Piccoli, 2020; Raimondo et al., 2017; Rubatto et al., 2020). To date, there is no free open source software that can create intensity maps, perform pixel classification, and offer quantification of element maps that are rigorously filtered for the LOD for each individual pixel.

This contribution presents a new measurement routine for quantitative compositional mapping by LA-ICP quadrupole MS (LA-ICP-QMS). An advanced data reduction environment is provided to process and calibrate the raw data embedded in the open-source and free software solution XMapTools (Lanari et al., 2023). The procedure involves the guided generation of intensity maps from time-resolved signals using an interpolation approach. Quantified elemental data for individual pixels are obtained by using an external standardization protocol combined with variable mass fractions of the element used for internal standardization, a previously unavailable prerequisite for minerals of variable compositions. The proposed procedure includes a rigorous calculation of the LOD for individual pixels. Three examples from metamorphic rocks are used to demonstrate the potential of this method for petrological applications.

Table 1
Definition of terms used in the text.

Term	Definition
Acquisition time	Total time of backgrounds and scan times for a given map.
Background	Gas blank measurement, usually around 30 to 50 s. This accounts for 11 to 30% of the total acquisition time (see text).
Dwell time	Net measurement time on one analyte (in s).
External standard	Material of known composition used for measurement calibration, following the IUPAC definition after Ettre (1993)
Fluence	On-sample surface energy density (in J/cm^2).
Internal standard	A known element mass fraction in the sample used to convert apparent element mass fraction obtained from external standardization into true sample element mass fraction, following the IUPAC definition after Ettre (1993)
Detector settling time	The time needed by the detector to go from one mass to the next in the element list.
Mask	Selection of an area of pixels by a particular shape.
Analyte	Isotope and element of interest set to measure in an element list in the ICP-MS software, corresponds to the m/z ratio of analyte = dalton.
Pixel	The spatial information of one value, such as a concentration, assigned in *X*–*Y* space.
Pulse	Application of the laser optical power for a duration on the sample.
Repetition rate	The number of laser pulses emitted per second (in Hz)
Region of interest (ROI)	An area of several pixels of interest sampled from the dataset.
Scan	Laser sampling in line scan mode.
Scan time	Time that laser is ablating and ICP-MS is recording.
Secondary standard	A reference material of known composition used for quality control purpose by comparison with a primary standard.
Spot	The shape of the laser beam here as a circular aperture (in μm).
Sweep	The acquisition of one full sequence of analytes in transient signal mode.
Sweep time	Total time in s required to measure all the analytes in sequence once
Transient raw signal	The raw data output as one continuous time-resolved record of analyte signal intensities.

2. Methods

2.1. Data acquisition

2.1.1. Time resolved analysis resolution

The sweep time of a given acquisition method controls the time resolved analysis resolution in a transient signal of a line scan. For LA-ICP-QMS, if long element lists are needed (>20 elements), the dwell times should be as short as possible to reduce artefacts caused by non-representative sampling (e.g., Pettke et al., 2000), and long enough to detect the element of interest. For a given analyte (i), the LOD can be calculated following Pettke et al. (2012):

$$LOD_i = \frac{3.29*\sqrt{\overline{I_i^{bkg}} \bullet DT_i \bullet \left(1 + \frac{N_i}{N_{bkg}}\right)} + 2.71}{N_i \bullet DT_i \bullet S_i} \quad (1)$$

where $\overline{I_i^{bkg}}$ is the mean intensity of the background (cps), DT_i the dwell time (s), N_{bkg} the number of sweeps for the background measurement, S_i the sensitivity of analyte i (in cps per μg/g of material), and N_i the number of sweeps for the measurement of the analyte in the sample. The numerical coefficients 2.71 and 3.29 relate to 5% probabilities of false positive and false negative detections as derived from a Poisson distribution (Pettke et al., 2012). The sensitivity S_i of the analyte is defined after Longerich et al. (1996):

$$S_i = \frac{I_{unk}^{int} \bullet C_{std}^{int} \bullet I_{std}^{i}}{C_{std}^{i} \bullet I_{std}^{int} \bullet C_{unk}^{int}} \quad (2)$$

with I as the intensity (cps) and C as the mass fraction (μg/g) of the internal standard element (int) in the external standard (std) and the unknown sample (unk). Increasing the dwell time and/or the number of sweeps of an element (i) results in a decrease of the LOD, keeping all other parameters unchanged.

2.1.2. Spatial resolution

The spatial resolution of the signal in X and Y directions are different and depend on the scanning direction (vertical or horizontal). Perpendicular to the scan direction, the spatial resolution is controlled by the beam diameter, while along the scan direction it is controlled by the number of overlapping pulses. This number is determined by the repetition rate, which is the product of the scan speed and the sweep time (Fig. 1). The scan speed v (expressed in μm/s) can be calculated as:

$$v = \frac{d}{n \bullet t_{acq}} \quad (3)$$

where d is the beam diameter (in μm), t_{acq} is the sweep time (in s), and n is the number of sweeps measured over a scan distance equal to the beam diameter. The spatial resolution along the scan direction is therefore directly proportional to the number of sweeps per scan distance. Fast scan speed is obtained for $n = 1$, corresponding to a single sweep acquired during a scan distance equal to the beam diameter (Fig. 1a). If n is >1, more than one sweep is acquired for a scan distance equal to the beam diameter (Fig. 1b), resulting in a higher spatial resolution along the scan direction. Spatial resolution is thus inversely proportional to scan speed, keeping all other parameters constant. At high scan speeds ($v > d/t_{acq}$) it has to be considered that the analytes are measured sequentially, the sweep and simultaneous stage motion results in a small shift of the spatial reference between the successively recorded analytes (Norris et al., 2021; Raimondo et al., 2017).

The compositional information of a given map is provided for each pixel individually that compose the map. The spatial resolution of the final map is defined by the pixel size. This differs from the spatial resolution of the signal discussed above. Different strategies can be used to convert the measured signal into pixel values. The first strategy is to assign an intensity value to a pixel for each sweep between the start and end positions during the scan. Square pixels are obtained if $n = 1$ (Fig. 1a) and rectangular pixels if $n > 1$ (Fig. 1b). This strategy is simple to implement and is used in IOLITE (Paton et al., 2011). Here, for circular laser beams, the material ablated in the outside half-circle at the start and end positions of the sweep is incorrectly included in the pixel value (Fig. 1b–c). A similar problem would occur if a square or rectangular beam shape were used. The second strategy is to apply

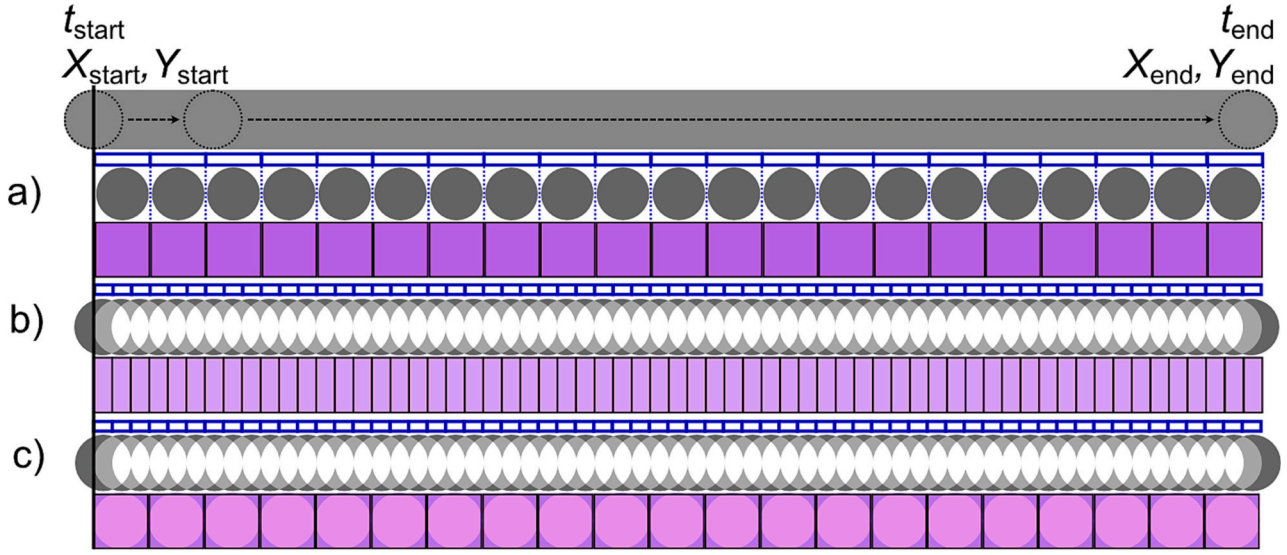

Fig. 1. Continuous line scanning with the laser in X and Y directions and pixel mapping. Three examples are illustrated using a fixed value for the total sweep and variable scan speeds and pixel reconstruction strategies. The values of t_{end} are different in (a) and (b) and the same in (b) and (c). The blue rectangles represent one sweep. The gray circles show the center position of the laser beam of each single sweep recording, and the purple squares show the shape and position of the pixels on the final map. (a) Fast scan speed resulting in a single sweep measurement for a scan distance equal to the beam diameter. The pixel allocation for the center position results in squared pixels of the same size as the beam diameter. (b–c) Slow scan speed resulting in three sweep cycle measurements for a scan distance equal to the beam diameter. Two pixel generation strategies are illustrated: in (b), a rectangular pixel is generated for each sweep, while in (c) squared pixels are obtained by interpolation across three sweeps for this example as implemented in this work (see text for further explanations). (For interpretation of the references to colour in this figure legend, the reader is referred to the web version of this article.)

oversampling in one or two dimensions and, additionally, signal deconvolution to reconstruct the true pixel intensity values from all individual measurements (van Elteren et al., 2021). This method offers a more accurate spatial resolution in the map, but has the limitation that the deconvolution process can lead to an increase in the signal uncertainty and therefore affect the precision of the measurement (van Elteren et al., 2021). The third strategy — the one developed here — is to use interpolation methods to transform the intensity signal into maps of square pixels using a value of n that is >1. A circular beam is used here because the energy density is more homogeneous for circular beams for laser systems relying on focusing (and not imaging) optics. In addition, the circular beam shape translates into a rectangular area when scanning in line direction (Fig. 1). Scanning over features that are smaller than the beam size will inevitably cause spatial resolution problems for either circular or rectangular beam shapes (see discussion).

2.1.3. Measurement of unknowns and standard materials

The map area of the sample is usually selected based on BSE images or composition maps obtained by EPMA. This area is scanned with horizontal or vertical lines, which are lined up touching each other. Ideally the scanning direction is perpendicular to the compositional features, offering better spatial resolution in the compositional map. A minimum resolution of 10,000 pixels (i.e., 100 × 100 pixels) is recommended for each map measured by LA-ICP-MS (Lanari and Piccoli, 2020).

The external and secondary standards used for calibration and quality control need to be scanned frequently to properly monitor instrumental drift (e.g., Longerich et al., 1996). In the proposed protocol, calibration is performed at least every 30 min at the exact same instrumental and data acquisition parameters. A minimum number of 100 sweeps for one line scan on the standard material is used to ensure a statistically meaningful measurement. The length of the line scan on the standard material is determined by the scanning speed and therefore the number of analytes and their dwell times (Eq. 2). In other studies, spot measurements were used to calibrate maps (George et al., 2018).

2.2. Map generation strategy and implementation in XMapTools

The data reduction scheme was implemented in the open source software XMapTools 4.3 (Lanari et al., 2014, 2019). Two modules have been developed for LA-ICP-MS applications: a converter module (Fig S2.4) and a calibration module (Fig. S2.5). The converter module includes signal intensity extraction, background correction, standard selection and interpolation, and intensity map generation. The calibration module is used for individual calibration of masked regions of pixels.

2.2.1. Converter module

Files containing the transient intensity data are imported together with a compatible laser ablation system log file. Automatic synchronization is performed by comparing the time of the first "laser on" state with the position — in time — of the first transient signal increase in the derivative of the total intensity signal. Signal intensities are then extracted from the raw transient signal by the defined time intervals for each background and line scan measurement for standards and unknowns.

A background correction is first applied and the detected background sweep cycles are interpolated over the time series for each element. Four interpolation methods are available to choose from: linear, polynomial (degree 2), step function, and a custom spline. The custom spline is obtained by cubic spline data interpolation. Signal integration intervals are selected automatically by excluding 10% of the total number of sweeps for the start and end of each background measurement. This value can be manually adjusted for all measurements. The start and end positions of individual background interval measurements can also be set manually. An automatic outlier rejection filter is also applied to each background measurement, rejecting any measurement that is >5 scaled median absolute deviation from the median value. The interpolation is then subtracted from the line measurement signal to generate background corrected intensity data, similar to procedures used in IOLITE (Paton et al., 2011) or SILLS (Guillong et al., 2008).

In the next step, one or multiple external standards are selected prior to map generation. Similar to the background selection, an automatic selection is made by excluding 10% of the total number of sweeps at the start and end of each measurement. Manual adjustment of this threshold is possible, as is examination of the signal and modification of the start and end positions of each selection. The four interpolation methods described above are available for external standard data interpolation.

A secondary standard is then used to verify the quality of the calibration. The selected secondary standard is automatically selected by excluding 10% of the sweep cycles at the beginning and end of each measurement. Once a primary and secondary standard have been selected, a comparison is made between the calculated (using the mean intensity value of all selected sweep cycles) and reference element mass fractions of the secondary standard by selecting an element for internal standardization.

Finally, for the unknowns, the start and end positions for each line scan is automatically selected to have an intensity signal that is consistent with the spatial position of the laser between scans. The map area is converted into a Cartesian grid of square pixels with a size equal to that of the beam diameter (Fig. 1). The grid is defined by positions corresponding to pixels. The intensity signal corresponding to each sweep is spatially referenced to the center position of the corresponding scan (Fig. 1). The resulting signal intensity grid has a different resolution along the scan direction when $n \neq 1$ (see Eq. 2). Intensities for the central position of each pixel on the map grid are obtained by interpolating the intensity signal grid surface using a gridded cubic interpolation of the non-zero measurements obtained via a Delaunay triangulation. This procedure is used to extract all data, the background intensity maps

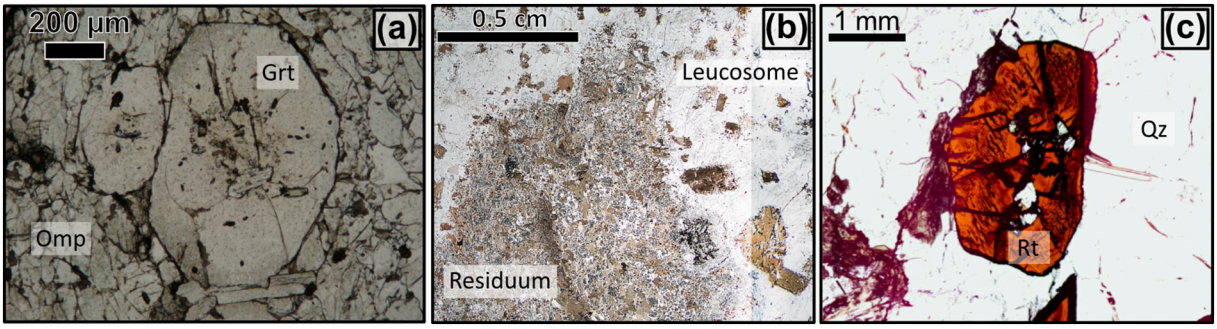

Fig. 2. Optical images of the (a) garnet DKE-352, (b) migmatite BA1013 and (c) rutile from sample AS19–3. a) Shows the targeted garnet grain in a matrix of pyroxene. (b) The residuum with higher biotite abundance next to the leucosome with larger biotite flakes but higher plagioclase abundance. (c) Image of the mapped rutile grain inside the matrix of quartz with visible exsolution needles of ilmenite. Mineral abbreviations are from Warr (2021).

from the interpolated background measurements and the intensity maps for standards and unknowns.

2.2.2. Calibration module

Masked regions of pixels corresponding to a single class (single phases, such as a mineral, glass or metal) within the intensity maps are calibrated individually using an internal standardization approach (Longerich et al., 1996):

$$\frac{C^i_{unk}}{C^i_{std}} = k\frac{I^i_{unk}}{I^i_{std}} \quad (4)$$

C^i_{unk} is the mass fraction of element (i) in the unknown sample, c^i_{std} the mass fraction of element i in the calibration material, I^i_{unk} is the intensity (cps) of element i in the unknown sample, and I^i_{std} the intensity (cps) of element i in the calibration material. The variable k represents the internal standardization factor and forms part of the relative sensitivity factor (RSF) following Halter et al. (2002):

$$k = \frac{I^{int}_{unk} \bullet C^{int}_{std}}{I^{int}_{std} \bullet C^{int}_{unk}}. \quad (5)$$

Pixels in the intensity map are calibrated using an analyte of known composition, i.e., the internal standard element (int), in a calibration material and the sample. Each calibration uses either a constant or a variable internal standard element mass fraction as selected by the user. A single value for the internal standard element mass fraction (i.e., c^{int}_{std}) is commonly used for calibration, but this strategy can only be applied to phases where the internal standard element mass fraction is constant across the phase in the mapped area. To calibrate inhomogeneous materials, a variable internal standard element mass fraction needs to be used. If the variation in the mass fraction of the internal standard element is known, the measured intensities in the map can be matched to the known mass fraction of the internal standard element. In both cases, constant or variable value, the composition is determined by an external technique or mineral stoichiometry, and is set as percent oxide weight which is automatically converted to μg/g element. The constant composition method applies this value to all pixels of the selected class regardless of the intensity value. The variable composition method uses a linear relationship between intensity and composition of the internal standard element. This relationship is manually defined by the user by selecting at least two regions of interest (ROI) and assigning a fixed composition value to each. This information can then be used for interpolation and calibration of materials with a variable internal standard element mass fraction. In addition, a choice of multiple external standards for individual element calibration has been implemented. While this approach is often used to calibrate LA-ICP-MS spot measurements to improve analytical accuracy, to our knowledge none of the mapping software solutions to date offer this feature. Different external standards can be selected by the user for different elements being sampled. Finally, the LOD maps are calculated using eq. 1.

2.2.3. Additional tools

Intensity maps can be used for phase classification using the machine learning algorithms implemented in XMapTools 4.3 (Lanari et al., 2023). The quantitative compositional maps obtained after calibration can be used for structural formula calculations and thermobarometry using functions from the PTtoolbox (Laughton, 2023). Advanced data interrogation is available using the sampling functions or the data visualization module of XMapTools (Lanari et al., 2014, 2019). A spider diagram module is also available and includes advanced tools for visualization and graphical representation or trace element data (Raimondo et al., 2017).

3. Application examples

Three case studies illustrated in Fig. 2 were selected to examine the workflow and calibrations, as well as measurement acquisition conditions and will illustrate selected aspects and benefits of our novel approach. The first example shows a comparison between fast and slow scanning speeds for mapping eclogitic garnets and omphacite from Lato Hills in Togo (maps 1.1, 1.2, and 1.3). The second example shows two multiphase maps acquired with different spatial resolutions of a migmatite sample from the El Oro complex in Ecuador (maps 2.1 and 2.2). This example contains minerals that show strong chemical zoning across the mapped area, thus requiring the variable composition method for internal standardization. The third case study provides trace element maps of rutile from Val Malenco in the Italian Alps used for thermometry (map 3.1).

Data reduction was performed entirely with XMapTools 4.3 (Lanari et al., 2023). Mineral classification was performed using the random forest algorithm. All data presented in this study, including the raw signal, the intensity and calibrated maps, are available in supplementary material 2 and in a Zenodo data repository (https://zenodo.org/doi/10.5281/zenodo.8340229).

3.1. Analytical conditions

3.1.1. LA-ICP-MS

Mapping experiments were performed at the Institute of Geological Sciences, University of Bern, using an ASI Resonetics RESOlution-SE 193 nm excimer laser system with the S155 dual volume sample cell coupled to an Agilent 7900 quadrupole mass spectrometer. The ablated material was transported from the ablation cell to the plasma in an atmosphere of He at a flux of 0.7 L/min mixed with Ar (0.86–0.87 L/min) and N_2 (0.003 L/min) at the exit of the ablation cell. At the beginning of each session instrument optimization included setting the ThO/Th intensity ratio to below 0.3% for low oxide production, and to ensure robust plasma conditions monitored by a U/Th sensitivity ratio of >0.97 (Günther and Hattendorf, 2005). The samples, consisting of polished thin sections (30 μm thick), were loaded into a spring holder of the S155 sample cell. The map areas were defined by a rectangular shape containing evenly spaced line scans using the GeoStar© software (Norris Scientific). A round aperture shape was chosen for all sessions to minimize variations in laser energy density across the beam area. The map size, laser beam diameter and scanning speeds for each map are given in Table 2. Detailed instrument conditions are given in supplementary material S1.

Each map acquisition contains line scans measured over standard reference material and unknowns, i.e., the samples. The sample surface was pre-cleaned prior to each line scan using an aperture one size larger than the beam diameter used for the map and a scanning speed 10 times the normal scanning speed. The data were acquired in transient analysis mode in one continuous acquisition. The following three reference materials were used to evaluate data quality GSD-1G, NIST SRM 612 and NIST SRM 610 (Jochum et al., 2005). For each mapping session, at least two of the three reference materials were used, so that always one primary and one secondary standard material were included (see Supplementary Material S1). Primary and secondary standard materials were measured with at least one scan every half an hour with a minimum distance determined by eq. 3 based on the scan speed in the respective experiment and acquiring a minimum of 100 sweep.

3.1.2. Electron probe micro-analysis

EPMA was performed using a JEOL JXA-8200 instrument at the Institute of Geological Sciences, University of Bern. Each EPMA session consisted of the measurement of spot analyses and X-ray maps. Analytical conditions for spot analyses were 15 KeV accelerating voltage, 10 nA specimen current and 40 s dwell times including 2 × 10 s of background measurement. Nine oxide compositions were measured using synthetic and natural standards as follow: wollastonite/orthoclase/garnet (SiO_2), orthoclase (K_2O), albite (Na_2O), magnetite/garnet (FeO, TiO_2), anorthite (Al_2O_3, CaO), forsterite (MgO) and tephroite

Table 2
Summary of applied LA-ICP-MS mapping conditions for application example 1 to 3. The dwell times used for each analyte are provided in Table S1.

Map	Map size [mm^2]	Map size $X \times Y$ [px]	Nb of pixels	Laser beam diameter [μm]	Scan speed [μm/s]	Time [hh:mm]	Surface energy [J/cm^2]	Nb of elements	Total sweep time [s]	Mineral	Primary Standard	Fraction of background measurement [%]	Internal Element Standard
Example 1 – Garnet DKE-350													
1.1	4	91 × 91	8281	12	7.5	03:20	5	38	0.46	Garnet	GSD-1G, NIST SRM 612	17.5	Ca
										Clinopyroxene	GSD-1G, NIST SRM 612		Ca
1.2	0.1	46 × 68	3128	5	3	02:50	5	19	0.51	Garnet	GSD-1G, NIST SRM 612	25.6	Ca
1.3	0.075	47 × 60	2820	5	3	03:00	5	19	0.51	Garnet	GSD-1G, NIST SRM 612	29.4	Ca
Example 2 – Migmatite BA1013													
2.1	4	165 × 37	6105	20	12	04:15	5	38	0.46	Plagioclase	GSD-1G, NIST SRM 612	15.0	Ca
										Biotite	GSD-1G, NIST SRM 612		Si
										K-feldspar	GSD-1G, NIST SRM 612		Al
2.2	4	330 × 60	19800	10	6	13:40	5	38	0.46	Plagioclase	GSD-1G, NIST SRM 612	11.8	Ca
										Biotite	GSD-1G, NIST SRM 612		Si
										K-feldspar	GSD-1G, NIST SRM 612		Al
Example 3 – Rutile AS19–3													
3.1	2.5	108 × 89	9612	16	10	06:54	5	26	0.32	Rutile	NIST SRM 610, NIST SRM 612	17.0	Ti

(MnO). Analytical conditions for mapping were 15 KeV accelerating voltage, 100 nA beam current and varying dwell times depending on the size of the map. Mapping with EPMA was performed to compare the element distribution obtained by mapping with LA-ICP-MS.

3.2. Sample description and map generation

3.2.1. Garnet DKE-352

Sample DKE-352 is a glaucophane-bearing eclogite from the Lato Hills, Togo. The observed mineral association consists of garnet (35–40 vol%), omphacite (15–20 vol%), glaucophane (10–15 vol%), zoisite (15–20 vol%), paragonite (<5 vol%), phengite (<5 vol%), quartz (10–15 vol%) and rutile (<5 vol%). Accessory minerals (<2 vol%) include apatite, zircon, allanite, titanite, ilmenite and hematite. The peak metamorphic minerals in this eclogite have recorded ultra-high pressure conditions of 2.8–3.0 GPa and 620–700 °C during the formation of the West Gondwana Orogen at ~610 Ma (Ganade de Araujo et al., 2014). The garnet grain recording the widest range of chemical variability in major elements from core to rim observed in sample DKE-352 was selected for the LA-ICP-MS analysis (Fig. 3).

Three LA-ICP-MS maps were collected on the selected garnet grain (Table 2). Map 1.1 (Fig. 5) was obtained with a spatial resolution of 12 μm to cover the entire grain and includes surrounding minerals such as pyroxene and mica. Map 1.2 and Map 1.3 (Fig. 5) were obtained one month later. Compared to map 1.1, a beam diameter of 5 μm was used to image the mantle to rim transition at a higher spatial resolution. Garnet in the three maps was calibrated using a variable composition of Ca used as the internal standard element. In each case the higher value of Ca was taken in the core area (78,617 μg/g Ca corresponding to 11.00 wt% CaO) and the lower value in the rim (42,882 μg/g Ca corresponding to 6.00 wt% CaO). These CaO contents were determined using average values for ROI in the major element maps obtained by EPMA.

3.2.2. Migmatite BA1013

Sample BA1013 is a migmatite from the El Oro Complex, Ecuador. The sample was collected in the pelitic domain of a metasedimentary xenolith embedded in the Marcabelli pluton (Riel et al., 2013). Two textural and mineralogical domains can be distinguished. (1) The biotite-poor (<15 vol%, grain size 0.5–1 mm) leucocratic domain accounts for ~45 vol% of the rock and is composed of K-feldspar (~35 vol%), plagioclase (~45%), biotite (<15%), quartz (<1%), ilmenite (<1%), magnetite (<1%), and apatite (<1%). This domain is interpreted as a result of partial biotite dehydration melting (Vielzeuf and Holloway, 1988) and referred to as the leucosome. (2) The biotite-rich (>30 vol%, grain size 100–300 μm) melanocratic domain makes up ~55 vol% of the rock and contains biotite (>30%), plagioclase (~55%), cordierite (~8%), spinel (~1%), apatite (<1%) and magnetite (<1%). This domain does not show evidence of melt and is referred to as the residuum. An area of interest was selected at the contact between the leucosome and the residuum (see Fig. 2 and 4a). The three main phases, plagioclase,

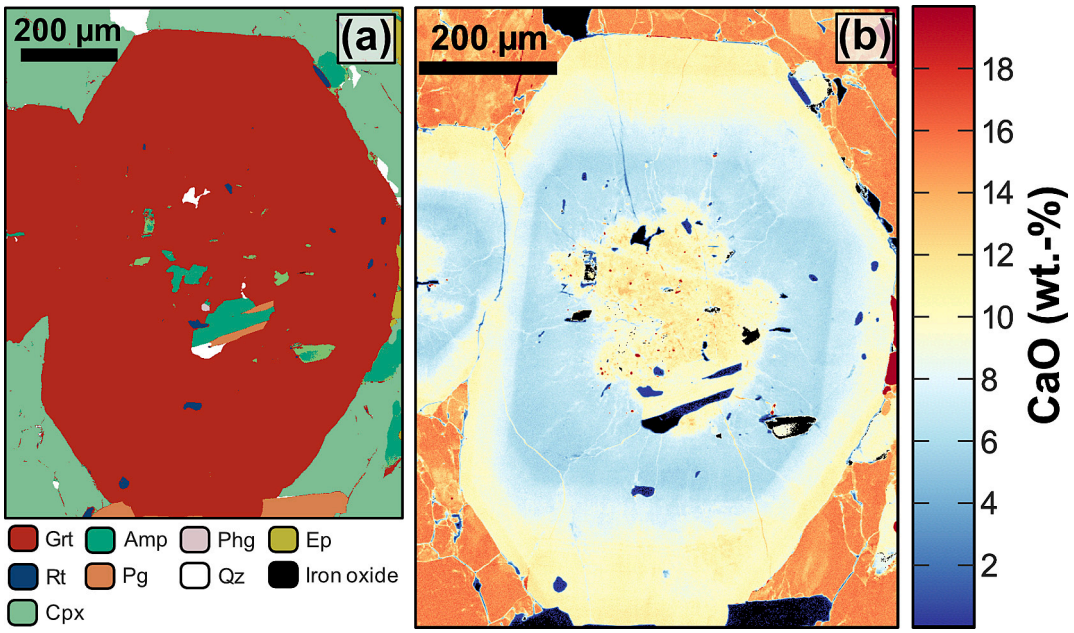

Fig. 3. Phase assemblage map (a) and major element compositional map of CaO in wt% for all phases (b) of sample DKE-352. (a) Shows inclusions of amphibole, rutile, and epidote in the garnet. (b) Garnet shows compositional variation between ~4 to 13 wt% CaO. All phases are calibrated separately (see text for more information). Mineral abbreviations are from Warr (2021).

biotite, and K-feldspar show major element variation. Plagioclase is strongly zoned in anorthite molar fraction from 0.1 to 1.0 (Fig. 4b), as reflected in major element variations (~10 wt% in NaO; ~20 wt% in CaO; ~15 wt% in Al_2O_3; and ~20 wt% in SiO_2). Biotite shows a variation of <2 wt% in SiO_2 and a higher variability of ~5 wt% in Al_2O_3. K-feldspar varies ~2 wt% in SiO_2, ~3 wt% in NaO and <1 wt% in Al_2O_3.

Two adjacent maps of 1 × 4 mm were obtained within the same area of the element maps from EPMA in two separate sessions. The first part map 2.1 was obtained with a spatial resolution of 20 µm and the second part map 2.2 with 10 µm in a separate analytical session, both covering the leucosome and residuum domains. Internal standardization of plagioclase was done with variable CaO mass fraction, because plagioclase contains no major element of constant mass fraction suitable for internal standardization with a constant value. For each map part, the minimum and maximum anorthite molar fraction in plagioclase (X_{an}) domains were defined as ROI for the calibration. Map 2.1 regions are in the high X_{an} domain (131,504 µg/g Ca corresponding to 18.40 wt% CaO) and low X_{an} next to the larger biotite grain (30,732 µg/g Ca corresponding to 4.30 wt% CaO). Map 2.2 regions relate to a medium-high X_{an} patchy domain at the contact between the two map parts (95,055 µg/g Ca corresponding to 13.30 wt% CaO) and a low X_{an} domain near the biotite flake (25,729 µg/g Ca corresponding to 3.60 wt% CaO). Calibration of biotite used Si as the internal standard element with a value of 166,861 µg/g corresponding to 35.70 wt% SiO_2. K-feldspar was calibrated using Al as the internal standard element with a value of 98,450 µg/g corresponding to 18.60 wt% of Al_2O_3. All values were determined using average values for ROIs in the major element maps obtained by EPMA.

3.2.3. *Rutile AS19–3*

The metapelite sample AS19–3 from Alpe Senevedo Superiore, Val Malenco (Italian Alps) reached high-pressure upper greenschist facies conditions of ~1.0 ± 0.3 GPa and 475 ± 25 °C (Bissig and Hermann, 1999). The observed mineral association consists of garnet (~10 vol%), chlorite (~15%), amphibole (~35%), quartz (~20%), white mica (~10%) and rutile (~10%). Rutile occurs as ~200 µm–sized grains within the matrix and can reach cm–sized grains within the quartz layer where the rutile contains ilmenite dissolution needles. The mapped rutile grain originates from the quartz domain (see Fig. 2).

A map of 2.5 mm^2 size has been acquired using LA-ICP-MS covering ~80% of the rutile grain shown in Fig. 2c. Rutile in the map was calibrated using Ti as internal standard element (599,260 µg/g Ti corresponding to 99.96 wt% of TiO_2).

4. Results

4.1. *Garnet DKE-352*

The results of structural formula calculations for garnet are shown in Fig. 5 and trace element maps in Fig. 6. Additional compositional maps are in the supplementary material S2. Major, minor, and trace element maps for pyroxene from both EPMA and LA-ICP-MS are provided in supplementary material S2 but not discussed here.

The maps of the end-member molar fractions (X_{alm} for almandine defined as molar Fe/(Fe + Mg + Ca + Mn); X_{sps} for spessartine as Mn/(Fe + Mg + Ca + Mn); X_{prp} for pyrope as Mg/(Fe + Mg + Ca + Mn); and X_{grs} for grossular as Ca/(Fe + Mg + Ca + Mn)) obtained by LA-ICP-MS are consistent with those obtained using the EPMA (Fig. 5). Distinct compositional zoning is observed between core, mantle and rim for X_{sps} and X_{grs}, whereas X_{alm} and X_{prp} show patchy distribution within the mantle. The X_{alm} LA-ICP-MS maps show slightly higher contents of ~1–3% in the patchy areas compared to EPMA data (Figs. 5a–d). Small veinlets connecting the outermost rim and the core of the garnet grain are observed in the X_{sps} map (Fig. 5e). The distribution of X_{sps} also shows an increase around the garnet core, separating core from mantle. These veinlets are still visible but not well resolved in the LA-ICP-MS maps, especially for the 12 µm resolution (Fig. 5f). The sharpness of the veinlets is improved in the maps obtained with 5 µm resolution (Fig. 5g). Faint oscillatory zoning is observed in the EPMA X_{grs} map (see arrow in Fig. 5m) but is not resolved in the LA-ICP-MS maps.

The garnet sample DKE-352 shows strong compositional zoning for most trace elements (supplementary material S2). A discussion of the systematics and differences between the LA-ICP-MS maps is based on Dy, Lu, and Y (Fig. 6a–f). An annulus is visible for Dy, Lu, and Y at the boundary between core and mantle. This feature is thin and sharp in the REE maps (e.g., Fig. 6a–c) and is positionally consistent with the

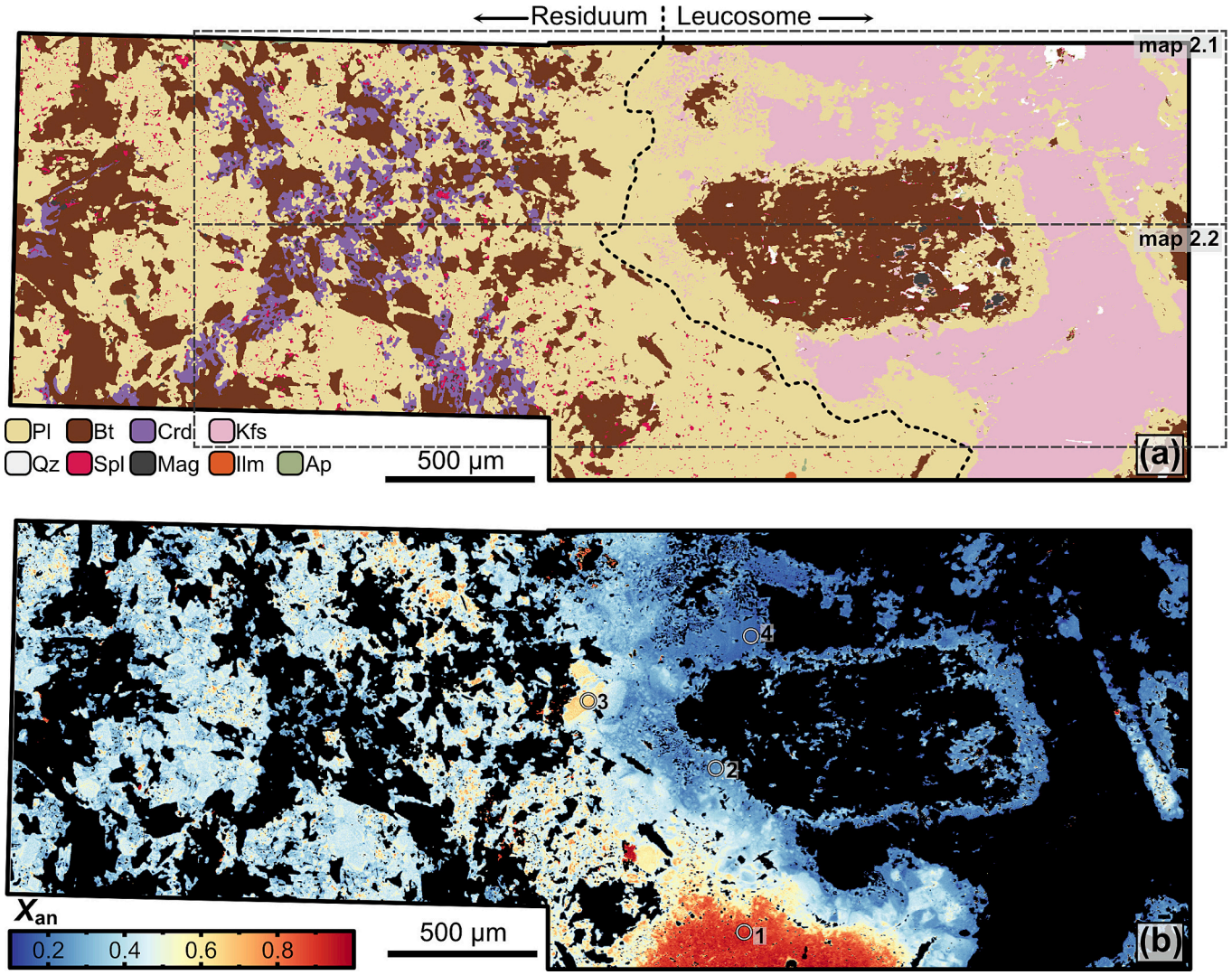

Fig. 4. Mineral phase assemblage map (a) and map of X_{an} (b) acquired with EPMA for plagioclase of the migmatite sample BA1013. The shape of the maps results from stitching of two subsets of maps from EPMA. (a) Showing the contact between the leucosome (right) and residuum (left). Inclusion phases in plagioclase smaller than 10 µm can be identified. Gray dashed fields represent the areas of map 2.1 and 2.2. (b) Strong zoning can be seen for X_{an} from almost pure anorthite to albite with a transition along the contact between residuum and leucosome. Circles define ROIs of extracted CaO mass fraction used for calibration. ROI 1 through 4 yield CaO values of 18.40, 4.30, 13.30, and 3.60 wt%, respectively. Mineral abbreviations are from Warr (2021).

manganese enrichment around the garnet core (Fig. 5e–h). Similarly, the transition between mantle and rim in the REE maps is sharper than that observed for the major elements. Furthermore, the elements Dy, Lu, and Y show a similar trend of increasing content from the inner rim to the outer rim and a sharp contrast between the mantle part wrapping the annulus and progressing towards the inner rim.

The three selected elements were reproduced between the three maps 1.1, 1.2 and 1.3. The average mantle composition in Dy is 19.5 µg/g for map 1.1, 17.9 µg/g for map 1.2 and map 1.3, and showing differences up to 8.5%. Values for Y decrease from mantle to inner rim from ~116 µg/g to ~25 µg/g in map 1.1 and from ~119 µg/g to ~24 µg/g in map 1.2 (similar for map 1.3), which corresponds to differences between map 1.1 and 1.2 of 2.5% and 4%, respectively. The average value of Lu in the mantle is 1.8 µg/g in map 1.1 and 1.9 to 2.0 µg/g in map 2.2 and 2.3 corresponding to a difference of 5 to 8%. A larger difference is found in Dy and Lu content of the annulus when comparing map 1.1 with map 1.2 and 1.3. Map 1.1 records generally lower values for the annulus with a maximum value of 58 µg/g whereas map 1.2 and 1.3 reach up to 75 µg/g. This is a difference of 25%.

Comparing the LOD of the pixels for the three elements between the three maps shows some expected differences related to the spatial resolution. The LODs are generally higher for the maps with the smaller spot size and this is visible in the Dy and Lu maps where some pixels in the garnet mantle region are below the LOD (see Fig. 6a–f). This is due to the fact that the mass of aerosol ablated per unit time increases with increasing pixel size (keeping all other parameters constant); hence, the LOD is inversely proportional to pixel size. The average LOD of Dy for map 1.1 is 0.9 µg/g, and for maps 1.2 and 1.3 it is 2.7 µg/g. The LOD of Lu is 0.2 µg/g for map 1.1, and 0.7 µg/g for maps 1.2 and 1.3. For Y it is 0.28 µg/g and 0.74 µg/g, respectively.

4.2. Migmatite BA1013

Compositional maps for biotite, K-feldspar, and plagioclase were generated using constant and variable mass fractions for the internal standard element (see above). Pixels corresponding to other phases (e.g., magnetite and cordierite) were not considered due to their mixed composition. The calibration procedure, including the generation of maps for LOD, is presented using the example of Ba for the two LA-ICP-MS maps (Fig. 7). The maps for major elements (CaO, Na_2O, Al_2O_3) and

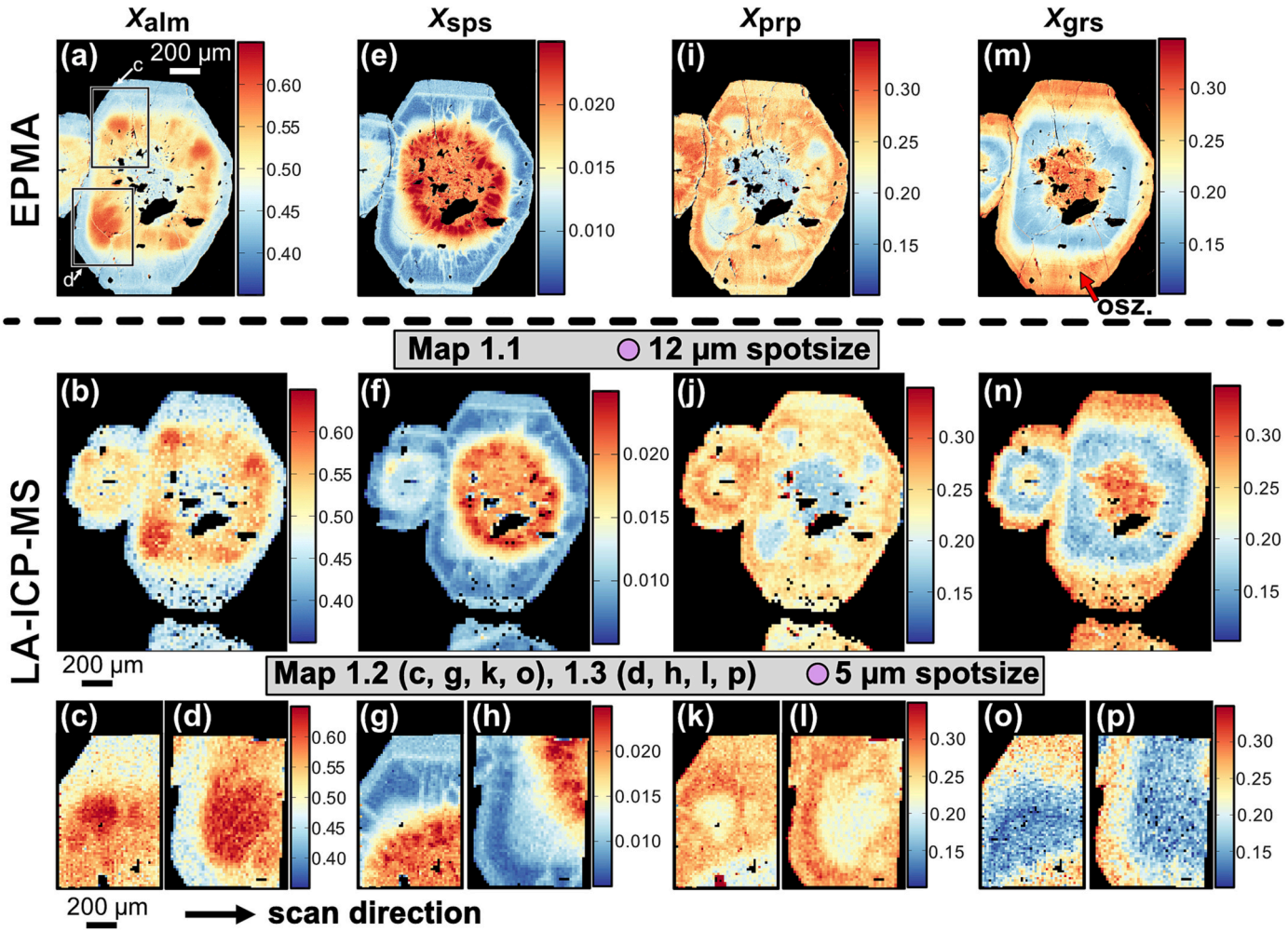

Fig. 5. Calculated end-member maps of X_{alm} (a–d), X_{sps} (e–h), X_{prp} (i–l) and X_{grs} (m–p) in garnet (DKE-352) for EPMA (a, e, I, m) and LA-ICP-MS mapping (b–d, f–h, j–l, n–p). (b, f, j, n) The results from mapping with 12 µm spot size. (c–d, g–h, k-l, o–p) The repeated mapping with a spot size of 5 µm. (a) Map of X_{alm} showing the sections of map 1.2 and 1.3 (black squares), which are shown in panel (c) and (d). (m) Oscillatory zoning is indicated in the garnet rim marked with the red arrow and acquired with EPMA. The scale shown is representative of all maps. (For interpretation of the references to colour in this figure legend, the reader is referred to the web version of this article.)

structural formula maps (X_{an}) for plagioclase obtained by LA-ICP-MS are then compared with EPMA data (Fig. 8). The comparison between EPMA and LA-ICP-MS data also includes maps of Ti-in-biotite thermometry (Fig. 9). Finally, results for selected trace elements are shown in Fig. 10. Additional maps of major elements, structural formulae and trace elements of plagioclase, biotite and K-feldspar are in supplementary material S2.

Map 2.1 was measured with 20 µm spot size and shows generally higher pixel intensities in Ba for all phases compared to map 2.2 which was measured with 10 µm spot size (Fig. 7b). After calibration no significant difference in major and trace element pattern is observed between maps 2.1 and 2.2 (e.g., Ba in Fig. 7c). Plagioclase shows a homogenous distribution of Ba (~300 µg/g), with the exception that lower contents (~70 µg/g) are observed in the high X_{an} domains (Fig. 4b). Biotite shows patchy Ba zoning especially in the larger grain located in the leucosome domain. K-feldspar shows both patchy zoning and domain zoning in Ba with a decrease of ~2000 µg/g between the upper and lower part of the leucosome. Note that the transition between these two K-feldspar compositions is not located at the boundary between the two maps. Calculated maps of LOD (Fig. 7d) show ~50% lower values in map 2.1 (20 µm) compared to map 2.2 (10 µm), again illustrating the inverse proportionality between pixel size and LOD for a given analytical protocol. The LOD map shown in Fig. 7d displays a pattern that reflects the different minerals present in the mapped area, because the ablation rate per unit time is variable for different minerals. As a consequence, the mineral-specific sensitivities for each analyte are variable for different minerals, resulting in variable LODs for the minerals mapped (keeping all other analytical parameters constant; compare eq. 1).

After calibration, an excellent agreement in composition is observed between maps 2.1 and 2.2 for major, minor and trace elements (Figs. 7, 8, 10), and between EPMA and LA-ICP-MS quantitative maps. The CaO maps of plagioclase obtained by LA-ICP-MS and EPMA record a compositional variation of ~20.0 wt% with a patchy zoning along the transition from residuum to leucosome (Fig. 8a, e). Plagioclase zoning in Na_2O shows ~10.0 wt% variation across the area for both LA-ICP-MS and EPMA maps (Fig. 8b, f).

Maps of LA-ICP-MS and EPMA show both illustrate the variation between almost pure anorthite and albite in the calculated map of X_{an}. Two selected ROIs show the local average value for X_{an}, one in the leucosome and one in the residuum area (see Fig. 8d, h). The value from EPMA results show in average 19% X_{an} (integrating 3400 pixels) and LA-ICP-MS shows 18% X_{an} (integrating 180 pixels) in the leucosome. In the residuum, X_{an} determined by EPMA is 63% (integrating 470 pixels) while that determined by LA-ICP-MS is 61% (integrating 21 pixels) on average.

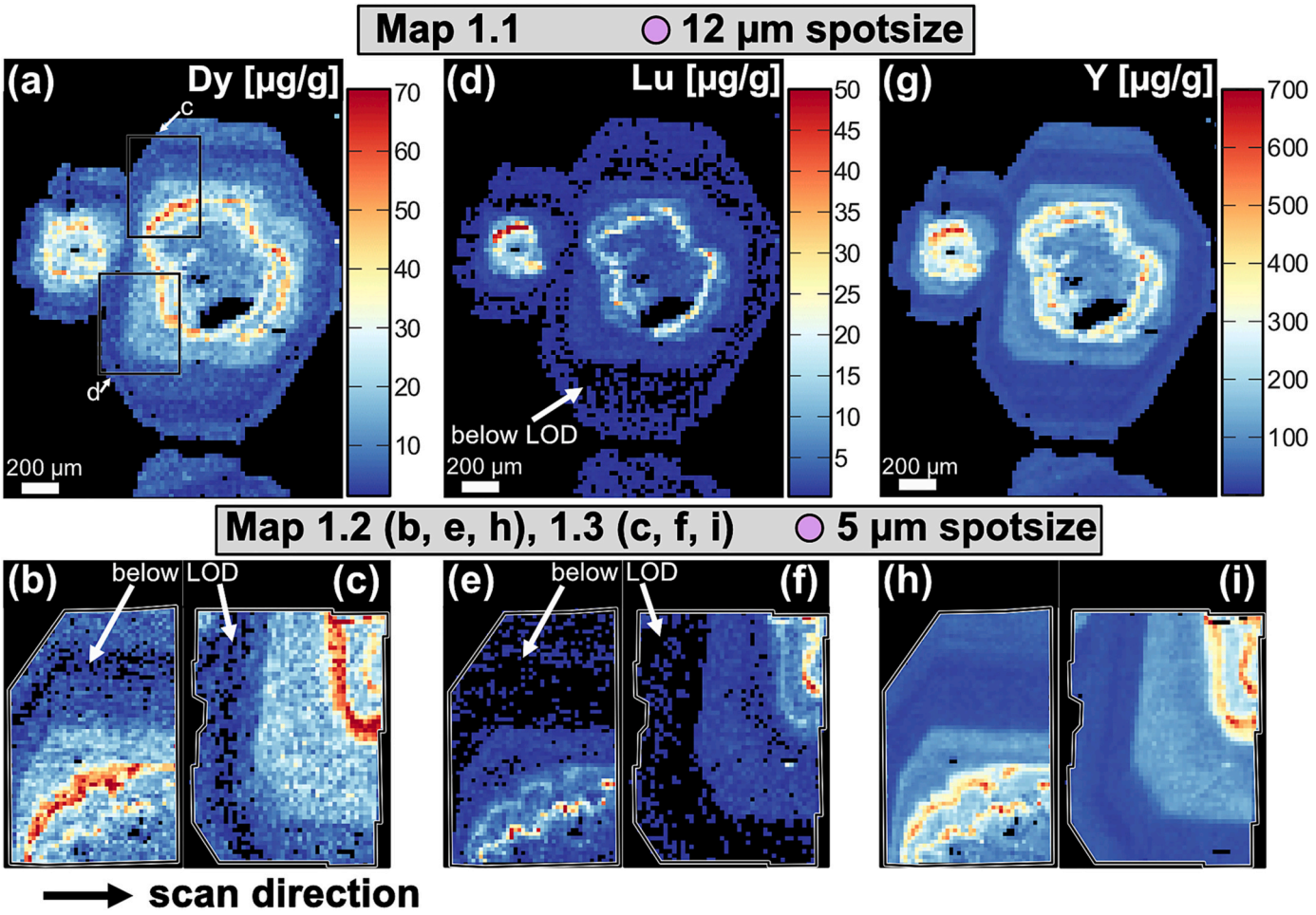

Fig. 6. LA-ICP-MS element maps for selected trace elements Dy (a–c), Lu (d–f), and V (g–i) in garnet (DKE-352). (a, d, g) Maps acquired with 12 µm spot size. (b–c, e–f, h–i) Maps acquired with 5 µm spot size. (b–c) Annulus shows higher content for Dy and a second annulus compared to the map in (a) acquired with lower spatial resolution. (b–f) A significant part of the pixels in the rim are black, representing pixels for which the apparent element mass fraction is below the corresponding LOD per pixel calculated individually for each element (white arrows). (b–c, e–f, h–i). The white line traces the grain boundary of the garnet.

The Ti-in-biotite temperature map obtained from EPMA results shown in Fig. 9a illustrates a gradual increase from left to right in the residuum domain from 600 to 700 °C. The large biotite flake in the leucosome domain yields the highest temperature of between 700 and 750 °C showing a slight irregular zoning pattern. LA-ICP-MS results illustrate the same gradual temperature increase in the residuum and similar zoning of the biotite in the leucosome (Fig. 9b). As a test, the same ROI in the EPMA and LA-ICP-MS maps return values for Ti, X_{Mg}, and temperature that are identical within analytical uncertainties (displaying a difference of 0.5%, 0.5%, and <0.2%, respectively).

Plagioclase, biotite, and K-feldspar show moderate to strong zoning in several trace elements as well as sectional differences between leucosome and residuum, which is shown using Sr in K-feldspar, Sr, La, and Nd in Plagioclase and Li, Co, V, and Rb in biotite (see Fig. 10). All trace element maps of K-feldspar, plagioclase, and biotite show no major difference at the boundary between the two maps 2.1 and 2.2, which were measured using the presented mapping routine with LA-ICP-MS but in separate analytical sessions (see Fig. 10 and S2.2). Instead, the generated maps resolve spatial patterns of trace element distribution in the different mineral grains and domains (Fig. 10 and S2.2).

4.3. Rutile AS19-3

Results of trace element distribution and a temperature map calculated using a Zr-in-rutile thermometer (Tomkins et al., 2007) are shown in Fig. 11. The element Ta is chosen as an example of observed trace element zoning in rutile. Additional trace element maps and temperature maps using additional calibrated functions are shown in supplementary material S2.

Sharp contrasts in the trace element patterns in rutile are shown using Zr and Ta (Fig. 11a–b). Zirconium and Ta are partially correlated, and the highest trace element contents are visible in a curved feature on the left side of the grain with ~70 µg/g Zr and ~190 µg/g Ta. The temperature map follows the Zr distribution with the highest temperature of ~550 °C in the curved feature and lower temperatures of 515–530 °C towards the rim.

5. Discussion

Six datasets including 19 to 38 measured elements resulting in a total of 178 intensity maps were acquired by LA-ICP-MS from three geological samples showing various mineral phases ranging across diverse metamorphic grades. Compositional maps were calculated from the time series intensity data using our novel data reduction protocol implemented in XMapTools. The following discussion focuses on the relevant features and advantages of our new method and the tools provided by our mapping approach, the resolution of the generated maps, and the quantification of element mass fractions and associated LODs calculated for each element per pixel as well as for ROIs. LA-ICP-MS mapping was compared with EPMA maps to evaluate the calibration quality.

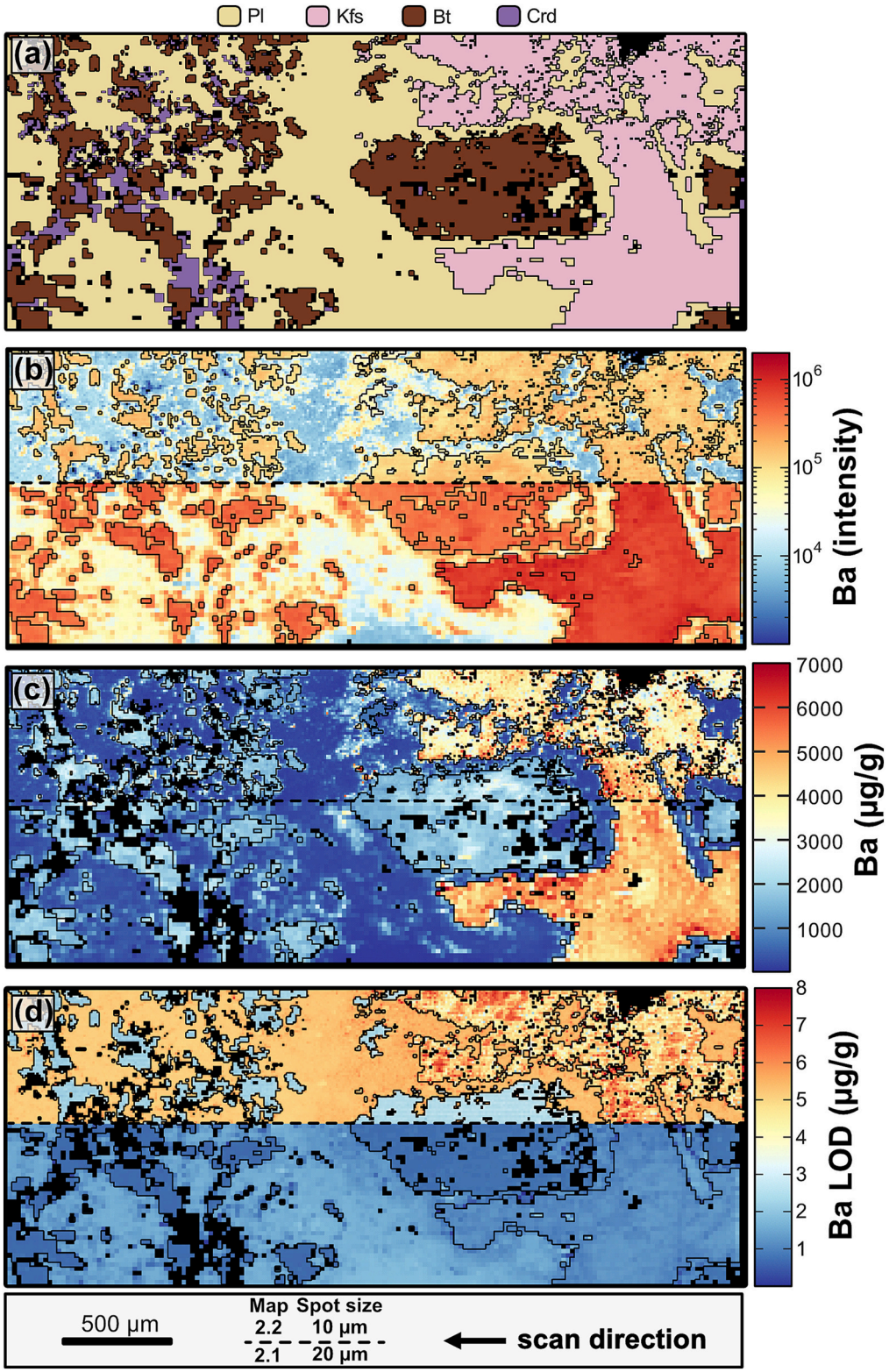

Fig. 7. Compilation of (a) the mineral assemblage, (b) the background corrected intensity map of Ba, (c) calibrated quantitative map of Ba and (d) map of the LOD per pixel for Ba in the phases of biotite, plagioclase and K-feldspar in sample BA1013. Lower half in the map represents map 2.1 using 20 µm spot size and the upper half map 2.2 using 10 µm spot size of adjacent domains in the sample. (b) The intensities in map 2.1 are larger by at least a factor of 2 compared to map 2.2, resulting from larger aerosol masses measured per unit time per pixel for the larger spot size. (c) After calibration, the interface between the two maps shows a smooth transition. (d) The LOD per pixel in the lower half of the map is roughly half the mass fraction of that in the upper half of the map. Black outlines have been added to highlight grain boundaries in all images in this figure. Mineral abbreviations are from Warr (2021).

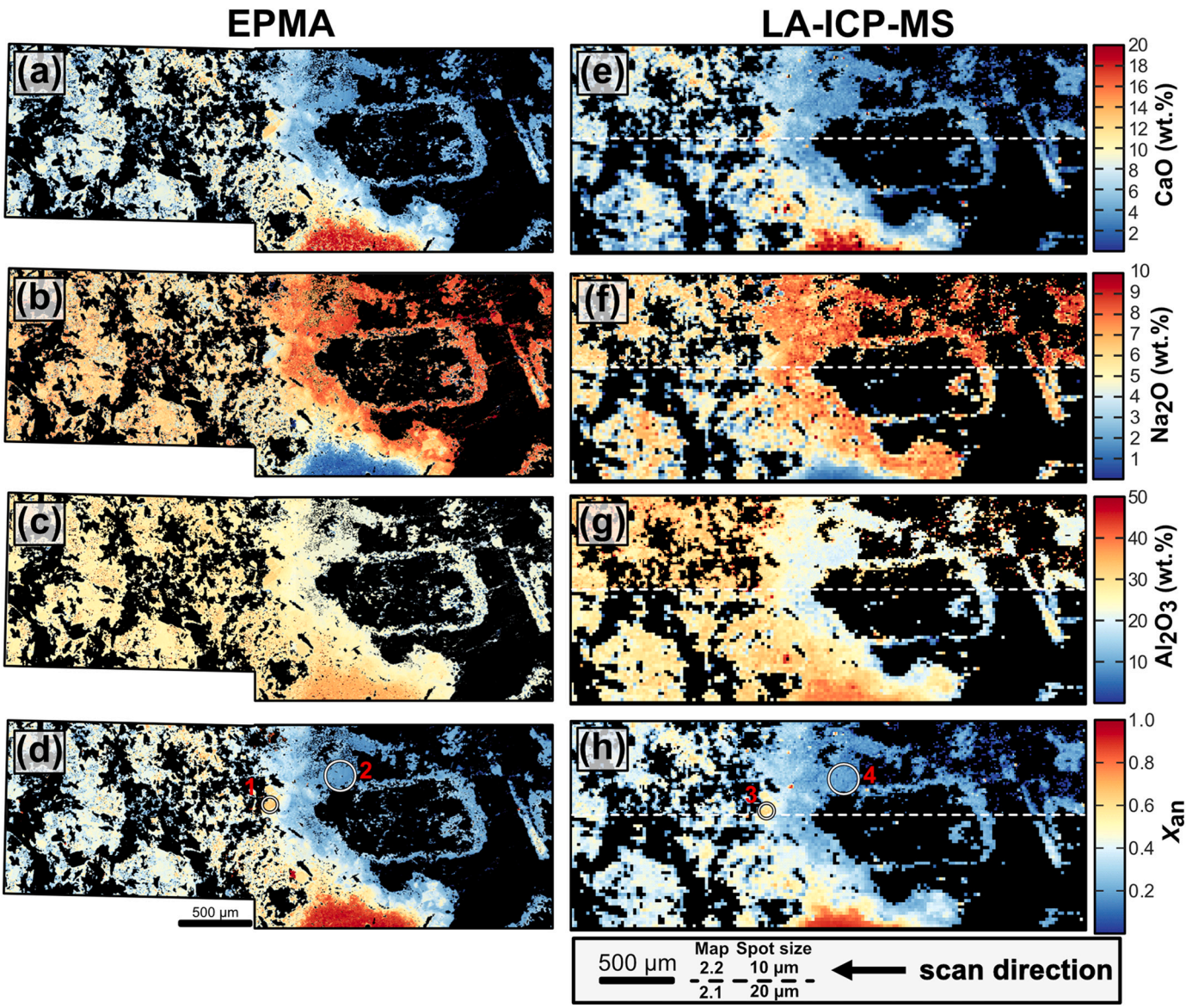

Fig. 8. Calibrated maps for plagioclase of CaO, Na_2O, and Al_2O_3 and calculated map of X_{an} maps for EPMA and LA-ICP-MS in sample BA1013. (d, h) ROIs in the leucosome and residuum represented as circles (1–4 in red). EPMA ROI 1 yield 0.63 (±0.05) X_{an} and 0.19 (±0.03) X_{an} for ROI 2 in leucosome and residuum respectively. LA-ICP-MS yield 0.61 (±0.03) X_{an} in ROI 3 and 0.18 (±0.03) X_{an} in ROI 4 for leucosome and residuum, respectively. (For interpretation of the references to colour in this figure legend, the reader is referred to the web version of this article.)

However, EPMA maps are not required and calibration of LA-ICP-MS maps can be done by single spot analyses or any other technique that can determine the internal standard element content used in the defined ROI.

5.1. Mapping method

High-resolution mapping of garnet (Fig. 6) can be performed at the same spatial resolution and similar detection power as recent LA-ICP-TOFMS experiments (Bussweiler et al., 2020; Rubatto et al., 2020). The acquisition rates calculated in this study using the total measurement time for standards and unknowns ranges between 15 and 40 pixels/min. This is similar to Raimondo et al. (2017) and significantly slower than LA-ICP-TOFMS (~170 to 3300 pixels/min in Rubatto et al. (2020) or ~1500 in Savard et al. (2023)). The acquisition rate of this study could be improved by reducing the number of sweeps per pixel. For $n = 1$, the acquisition rate would be between 45 and 120 pixels/min. This is still lower than what was reported by Konrad-Schmolke et al. (2023). Similar figures could be obtained by reducing the duration of the background measurement, which accounts for 11 to 30% of the acquisition time in our data acquisition procedure and depends on the scan duration of a single line (Tables 1 and 2) and the duration of the washout (1.4 to 7.9%). The duration of the background measurement could be reduced; however, this results in higher LODs, if all other parameters are kept constant (see Eq. 1 and Fig. S2.6).

Each mapping experiment requires ascertaining the balance between spatial resolution and compositional detection capability. Maps can be collected faster by increasing the spot size. In the example of the migmatite sample BA1013, the beam diameter of map 2.1 is twice that of map 2.2, allowing mapping to be performed 3 times faster. The loss in spatial resolution is moderate because similar zoning patterns could be resolved in the composition for minerals, especially for large grains at least 20 times the diameter of the laser beam. However, this depends on the size of compositional zoning features and thus also on the grain size of the target area. For example, a 500 µm biotite grain and its internal chemical zoning are reasonably well resolved when imaged with a 20

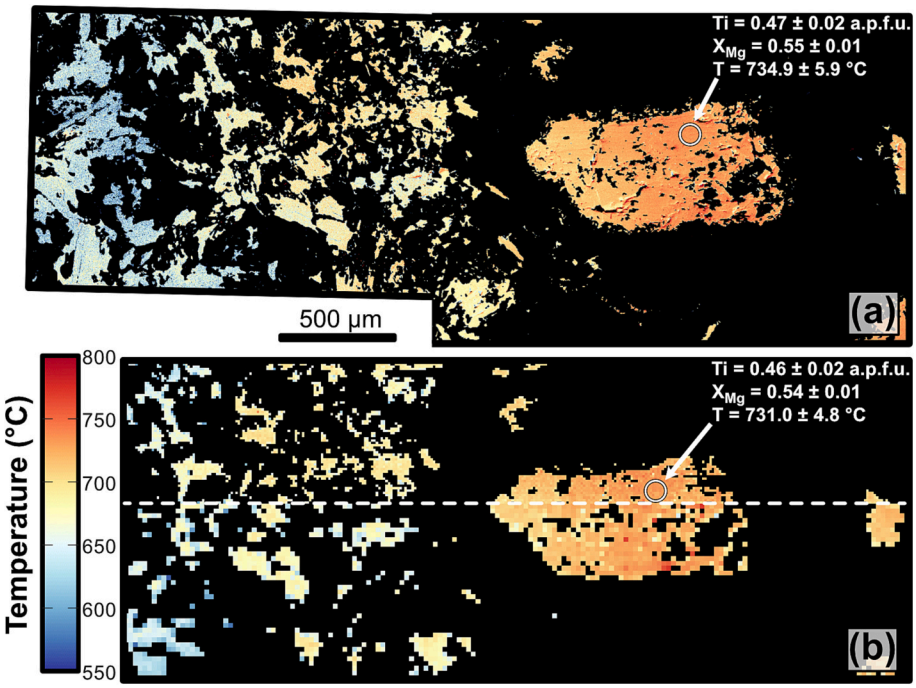

Fig. 9. Temperature maps of biotite calculated using the Ti-in-biotite thermometer of Henry et al. (2005) obtained by (a) EPMA, (b) LA-ICP-MS in sample BA1013. The comparison of results for the same ROI (white circle) in the large crystal of the leucosome reveals that calculated temperatures are identical within uncertainties for the EPMA and LA-ICP-MS maps. Mean and standard deviation values were obtained from the pixel values within the circular ROI. The measurement precision of the LA-ICP-MS temperature determination ($2\sigma = 0.65\%$) is slightly higher than that of the EPMA determination ($2\sigma = 0.8\%$).

µm beam diameter (Fig. 10). Grains smaller than 400 µm are better resolved in the 10 µm spatial resolution map as only then can similar features be resolved as in EPMA maps (Fig. 8). Spatial resolution of maps is inversely proportional to LOD of the analytes per pixel. Larger beam diameters (= poorer spatial resolution) result in a significant gain in detection power as illustrated by the LOD value (Fig. 7d). As a result, more pixels are generally below LOD when a higher spatial resolution — i.e., a smaller spot size — is used (Fig. 6), and analyte mass fractions near the respective LODs are measured less precisely. Increasing the resolution by a factor of 2 (e.g., from 20 µm to 10 µm) will increase the measurement time by 3 to 4 times and double the respective LODs.

5.1.1. *Precision and accuracy*

The maps of samples DKE-352 and BA1013 are useful to evaluate the precision and accuracy of our mapping approach. Accuracy was assessed for major and minor elements by comparing LA-ICP-MS maps to EPMA maps (see Figs. 5 and 8). We recall that a well-calibrated QMS instrument is necessary for the testing process, notably the calibration of the pulse to analog detector signal conversion factor. The three maps of sample DKE-352 and the two maps of sample BA1013 were acquired with different measurement conditions (on different days; Table 1). Quality tests on secondary standards (GSD-1G, NIST SRM 610 and NIST SRM 612) returned mass fraction data in the maps that are generally within 10% of preferred values (see supplementary material S1), demonstrating accuracy of our mapped element mass fraction data. Moreover, our maps also document excellent external reproducibility, as merged compositional maps do not reveal measurement day dependent content jumps or other differences in patterns.

The LA-ICP-MS major element maps reproduce the maps obtained by EPMA, illustrated by identical zoning patterns and element mass fraction data that differ by <10%, mostly identical to within a few percent. The accuracy of LA-ICP-MS mapping was tested by structural formula calculations for sample BA1013 using CaO mass fractions for internal standardization of the LA-ICP-MS maps. The EPMA structural formula calculations are known to have a precision of ~1%. The X_{an} of plagioclase is within 3 to 5.5% between EPMA and LA-ICP-MS data (Fig. 8). Part of the differences can be explained by the lower spatial resolution of the LA-ICP-MS maps. This is the case for the ~100 µm wide albite-rich plagioclase domain surrounding the large biotite grain in the leucosome. Map 2.1, obtained with a spot size of 20 µm, shows a close agreement with the EPMA results, with only a few percent difference compared to the EPMA data, and the higher spatial resolution map 2.2 shows even better agreement with the EPMA data, with a difference of <5% in X_{an}. The larger difference in the low spatial resolution map can be explained by the presence of pixels representing a mixed composition between plagioclase, biotite and K-feldspar. For samples DKE-352, the end-member fractions of garnet obtained by EPMA and LA-ICP-MS mostly agree to within 5%. Zoning domains that are smaller than 200 µm can show slightly higher difference below 10%. This differences can also be explained by the larger beam diameter of the LA-ICP-MS, between 5 and 14 times larger than the 1 µm beam size used for EPMA mapping.

Another test was performed using the Ti-in-biotite thermometer of Henry et al. (2005) for the migmatite sample BA1013. The reference material GSD-1G was used as the external standard and Si as the internal standard element, resulting in a biotite temperature of 731.0 ± 4.8 °C (Ti = 0.46 ± 0.02 apfu; X_{Mg} = 0.54 ± 0.01) with LA-ICP-MS extracted from the circular ROI. The average temperature of the selected ROI shows a difference of ~4 °C compared to EPMA results. This is well within the respective measurement uncertainties of EPMA and LA-ICP-MS and smaller than the uncertainty inherent in the calibration of the Ti-in-biotite thermometer by Henry et al. (2005). In contrast to the eclogite sample DKE-352, which is externally standardized to NIST SRM 612, the X_{Mg} of biotite is more reliably determined using GSD-1G as an the external standard because the calibration for Mg and Fe is better when high-Mg-Fe standards are used. Moreover, the map of sample BA1013 calibrated using NIST SRM 612 as the external standard results in an average biotite temperature of 775.2 ± 4.3 °C for the ROI shown in Fig. 9 (Ti = 0.49 ± 0.02 apfu; X_{Mg} = 0.69 ± 0.01), 44 °C higher than that obtained by external standardization on GSD-1G. These differences

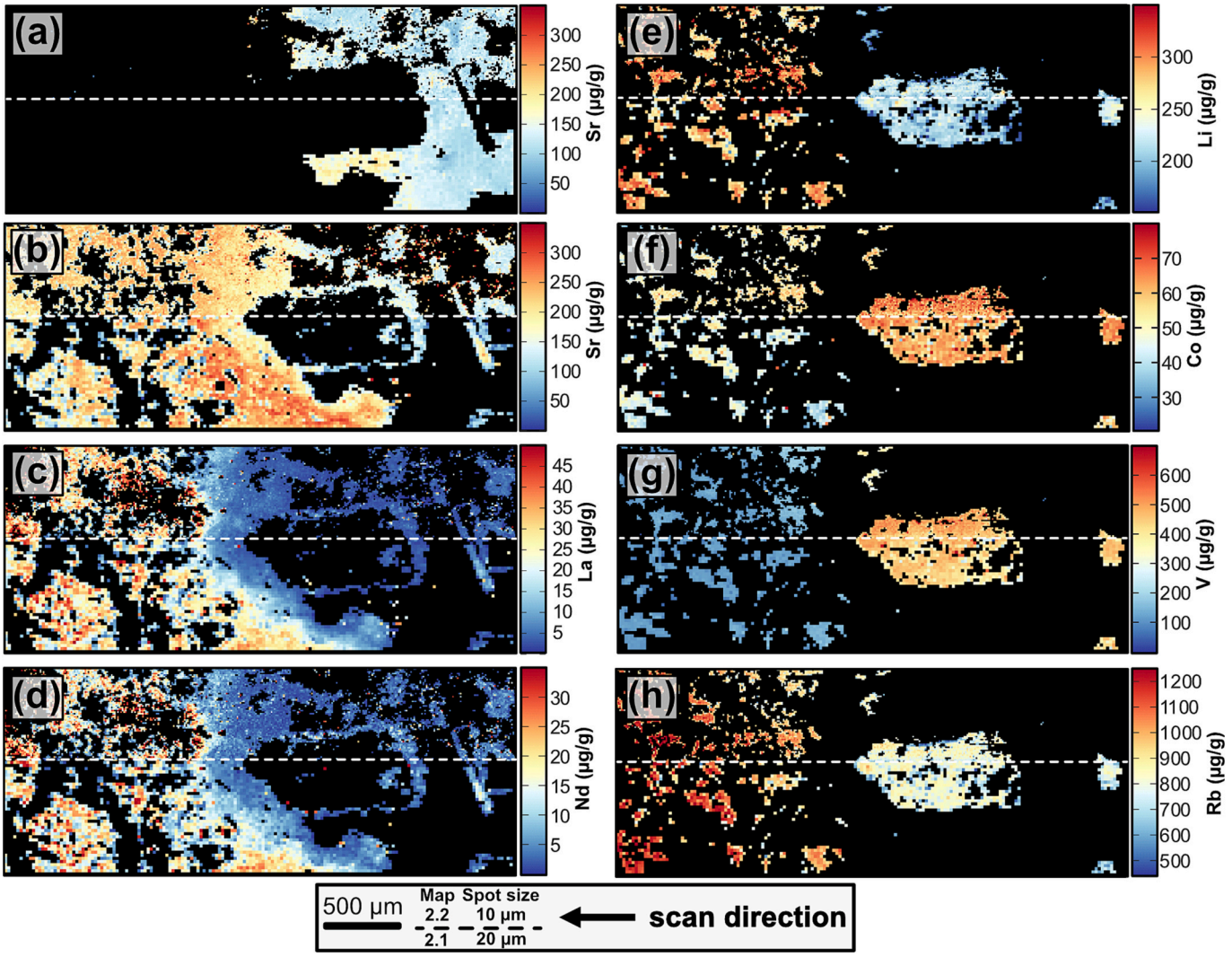

Fig. 10. Quantitative trace element maps obtained by LA-ICP-MS (a) Sr in K-feldspar, (b–d) Sr, La, and Nd in plagioclase, and (e–f) Li, Co, V, and Rb in biotite of sample BA1013. Colour codes represent element mass fractions per pixel while black pixels in the map represent apparent element mass fractions below the respective LODs calculated individually for each element in every pixel.

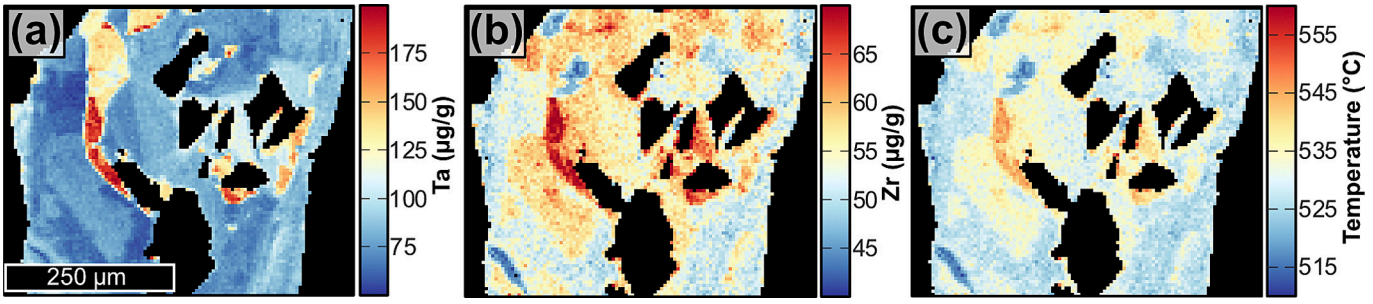

Fig. 11. Trace element maps of Zr and Ta in rutile and temperature map of rutile calculated using the Zr-in-rutile thermometer of Tomkins et al. (2007) obtained by LA-ICP-MS. (a–b) The elements Ta and Zr show a patchy zonation with no correlation to the cracks visible in Fig. 2c. (c) The temperature map shows variation in the temperature of maximum ~7.5% difference, from ~510 to 550 °C. Black map domains represent other phases.

illustrate well the limited reliability of NIST SRM 612 external standardization for Fe, Mg, Ti, and, by implication, for other major/minor elements that are present in NIST SRM 612 at ca. 40 µg/g mass fraction only. This is why we use GSD-1G for external calibration, which has a basaltic major and minor element composition. Importantly, it also emphasizes the benefit of using different external standards for different elements as implemented in XMapTools, to improve the accuracy of LA-ICP-MS map calibration for compositionally diverse minerals covering a wide range of element contents.

The accuracy of the LA-ICP-MS map calibration for trace elements presented in this study compares favorably to the accuracy obtained for single-spot measurements using the same reference material for external standardization and employing the same element mass fraction for internal standardization. In sample DKE-352, the trace element mass

fractions obtained for all maps are consistent within ±3% for Yb, Er, Y, <10% for Sc, V, Cr, Dy, Ho, Lu and < 15% for Tm. Similarly to major elements, compositional zoning patterns smaller than 100–150 μm are visible and show more extreme differences (e.g., maps 1.2 and 1.3 in Fig. 6) due to the spatial resolution effect discussed above. An interesting feature is the REE-rich annulus where two key differences can be seen in the trace element maps (Fig. 6). First, the maps 1.2 and 1.3, which represent a higher spatial resolution, consistently show higher contents when compared to map 1.1, which was obtained with a lower resolution. For example, measured Dy content increases from 58 to 75 μg/g corresponding to a 25% increase with increasing annulus thickness. The second ring of the annulus is almost absent in map 1.1 due to the lower spatial resolution. The second difference is best observed in map 1.2, where Dy reaches values of 50 μg/g when the annulus is oriented perpendicular to the scanning direction and 58 μg/g (corresponding to a difference of 14%) when oriented parallel to the scanning direction. Clearly, mapping at lower spatial resolution was insufficient to fully resolve the narrow high-content zone, as further evaluated in the next section.

5.1.2. Pixel allocation and direction of scanning

The ultimate aim of 2D mapping is the spatial presentation of element content data via the assignment of pixels on a two-dimensional grid. The approach proposed in this study involves generating square pixels from a line scan using an interpolation method, as opposed to the rectangular pixels commonly employed in other software (Chew et al., 2021, and references therein). The interpolation method allows to minimize the number of incorrectly assigned laser pulses to each pixel (see van Elteren et al. (2019) and Fig. 1). Fig. 12 illustrates different results of converting the intensity signal of one single scan into an intensity map. The intensity measurement for each sweep (black dashed line) can be averaged or interpolated to obtain square pixels. Alternatively, averaging of sweeps is used, for example, in the CellSpace software solution (Paul et al., 2012). In the case of an annulus or any other type of narrow feature that generates a high-intensity signal measured by a single sweep, the interpolation method is much more precise than the averaging method (Fig. 12). However, the gridded cubic interpolation via the Delaunay triangulation method was used in this work due to better performance in the numerous 2D maps generated during this study. Importantly, we recommend to use three sweeps for each squared pixel ($n = 3$ in Fig. 1a). If three sweeps are integrated into a squared pixel, a sufficiently slow scanning speed is required to obtain the resolution of chemical features for the given spatial resolution. This approach cannot resolve features smaller than the spot size, as other studies have also noted (Jollands, 2020; van Elteren et al., 2021). Importantly, interpolation methods allow for representative recording of fast transient signals, thus avoiding potential problems with aliasing, as previously reported for other strategies (Norris et al., 2021; Van Malderen et al., 2018). Moreover, including multiple sweeps in a single square pixel also reduces the element LODs per pixel, thus significantly improving element detectability for our LA-ICP-MS mapping protocol. The data reduction method implemented in XMapTools has the flexibility of using any value of n, the number of sweeps per square pixel, which is determined by the user's LA-ICP-MS setup as detailed above. The interpolation is performed on a rectangular Cartesian grid with a pixel size equal to the beam diameter. In practice, the scanning speed and the number of sweeps integrated into one squared pixel can be calculated by utilizing eq. 3.

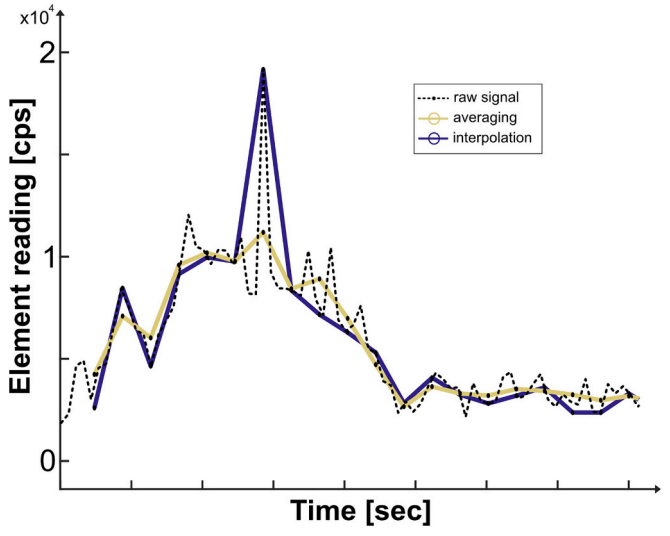

Fig. 12. Transformation of the raw intensity signal to intensities used for maps, based on a single-scan example. The method of the commonly used average (yellow line) and interpolation method presented in this work (blue line) are shown for comparison. Both interpolation and averaging take three raw signal measurements into account before transforming them to one value. (For interpretation of the references to colour in this figure legend, the reader is referred to the web version of this article.)

We developed a virtual mapping example to further illustrate and quantify the potential artefacts of the interpolation approach. A "real intensity map" is created with an ultra-high resolution (1×10^{-2} μm). This program measures the intensity acquired for a given beam size and scan speed by averaging a shape corresponding to the scanned surface of each sweep. It simulates the results of a measurement from a LA-ICP-MS system, and the data extracted from the simulation underwent the same interpolation approach as implemented in XMapTools. In Fig. 13, a band of 10 μm width oriented perpendicular to the scanning direction is shown, which has a pixel value of 34 μg/g. Each experiment has a fixed value of 3 sweeps per pixel ($n = 3$). If the beam size is twice the width of the band, the maximum intensity is reduced by ~33% and the distance of a mixed signal intensity into the pixel is roughly 3 times the width of the band. When the beam size is similar to the width of the band the true feature size is measured whereas the maximum intensity is still reduced by ~5%. The slight increase in the measured intensity before the annulus also shows a possible smearing effect which still occurs with similar spot size to the feature. Our finding is consistent with the results on analytical convolution artefacts presented by Jollands (2020). As shown in the maps of sample DKE-352, the true composition of any feature can be resolved for cases where the feature size corresponds to at least two times the beam size. For pure scanning perpendicular to mineralogical or chemical features, the use of rectangular beam shapes can help in their spatial resolution (e.g. Jollands, 2020). In theory, the presented interpolation method can spatially resolve the true composition of features as small as the beam diameter, but with a subordinate smoothing effect (Fig. 13c).

5.1.3. Determination of element-specific LOD per pixel in LA-ICP-MS maps

Quantified element maps are effective at showing regions of similar composition and relative differences such as zoning patterns as shown in several published studies (Ahmed et al., 2020; Bovay et al., 2022; Bussweiler et al., 2020; Drost et al., 2018; Fox et al., 2017; Gaidies et al., 2021; George et al., 2018; Gundlach-Graham et al., 2018; Hagen-Peter et al., 2021; McCarron et al., 2014; Paul et al., 2014; Petrus et al., 2017; Piccoli et al., 2022; Raimondo et al., 2017; Rittner and Müller, 2012; Savard et al., 2023; Tamblyn et al., 2021, 2020; Tual et al., 2022; Ubide et al., 2015; Ulrich et al., 2009; Woodhead et al., 2016). However, none of the cited studies compute LOD maps and only a few filter the quantified maps to assess which pixel values were detected at statistically defined confidence. To date, only Gundlach-Graham et al. (2018) have calculated the LOD per pixel using a single laser pulse and filtering resulting maps. Rubatto et al. (2020) developed an approach to determine the LOD per pixel based on the mass removed per pixel in the sample. Additionally, Rittner and Müller (2012) discard pixels with values below an average LOD. Other studies have only defined regions

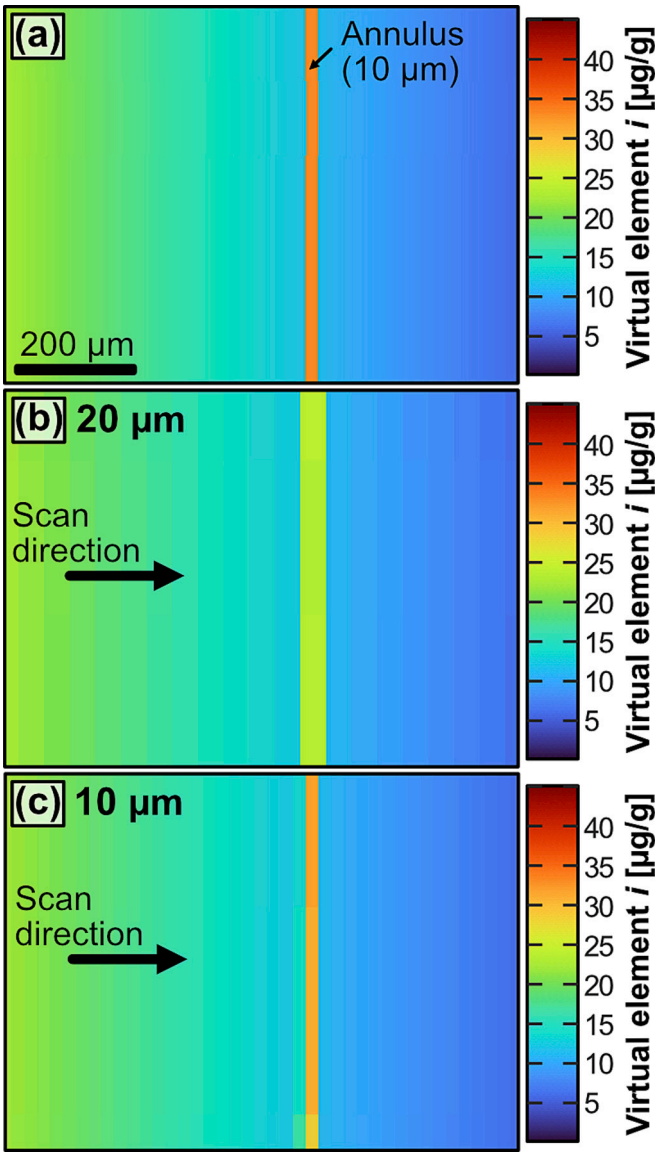

Fig. 13. Virtual mapping of an annulus of higher content with different spot sizes. (a) The virtual distribution of element *i* in a phase is shown with a band width of 10 µm and a composition of 34 µg/g. (b) Virtual results from scanning with LA-ICP-MS using a spot size of 20 µm. (c) Virtual results from scanning with LA-ICP-MS using a spot size of 10 µm. (b-c) Direction of scanning is from left to right in the images (black arrow).

within the mapped areas, extracted the data, and calculated the LOD or limit of quantification (LOQ) from such ROIs (Petrus et al., 2017; Raimondo et al., 2017; Zhu et al., 2016). Conversely, the LOD calculation presented in our work is based on eq. 1 proposed by Pettke et al. (2012) and provides the LOD for each pixel at 95% confidence in a classified and calibrated phase. The magnitude of the LOD is dependent on the number of sweeps in each pixel and the sensitivity during measurement, and the user can influence this by selecting appropriate map measurement settings. The software XMapTools allows the user to view each LOD map calculated for each element individually, and the final maps can then be filtered for LOD by user selection.

Mapping experiments in this study included up to 38 analytes in the element list and no measurement artefacts are detected in the generated maps. Low abundance elements in the mapped phases may go undetected (as they are below the LOD) depending on the sampling parameters (Fig. 6 and supplementary material S2). Maps of Ba in sample BA1013 show that the sampling parameters influence the LOD, as expected (Fig. 7d). The 20 µm spot map has an LOD of ~3 µg/g for Ba and is half the LOD calculated for the 10 µm spot size map. Variations in the LOD values are the result of the sensitivity factor and therefore the pixel intensities recorded (see Eq. 1). The Lu maps in garnet from sample DKE-352 provide an example of when the LOD is reached for domains of relatively low Lu abundance (Fig. 6d–f). In the case where no filter is applied for the pixels, Lu appears to be detected in low abundance domains and may even resolve a zoning pattern, although the average LOD for Lu is 0.2 µg/g for the map 1.1 and 0.7 µg/g for map 1.2 and 1.3. Similarly, Raimondo et al. (2017) present continuous zoned maps of Lu in garnet that reach low values of Lu with values below 1 µg/g. Filtering the image for pixels that are below the calculated LOD identifies ~6% of the REE pixel data as non-significant in map 1.1 (Fig. 6d) and ~35% in maps 1.2 and 1.3 (Fig. 6e–f), all displayed as black pixels. Maps are intended to guide the eye to read chemical information; therefore, we consider filtering pixels for LOD to be mandatory for removing potentially misleading information. An LOD filter represents a prerequisite for preventing data below the LOD from being interpreted (see examples in Figs. 14 and 15).

5.2. Application examples

Major and trace element mapping is essential to resolve, recognize, and interpret spatial variations in geochemical patterns, to eventually better understand petrogenetic processes. With the three application examples presented we now showcase the potential of multi-mineral mapping for the investigation of metamorphic processes.

5.2.1. Garnet DKE-352

Spatial correlation of chemical signatures in garnet has the potential to reveal mechanisms of crystal growth, recrystallization and resorption, element diffusion, elemental (re)distribution and open-system processes during metamorphism (George and Gaidies, 2017; Raimondo et al., 2017; Rubatto et al., 2020). For example, major and trace element maps show that the garnet in sample DKE-352 contains concentric zoning (Figs. 5 and 6). The garnet core major element zonation patterns (Ca, Mn) correlate with enrichments in V and Cr (and to a lesser extent Ti and Zr; Fig. S1) and low Lu, Dy, and Y contents (Figs. 5 and 6). The

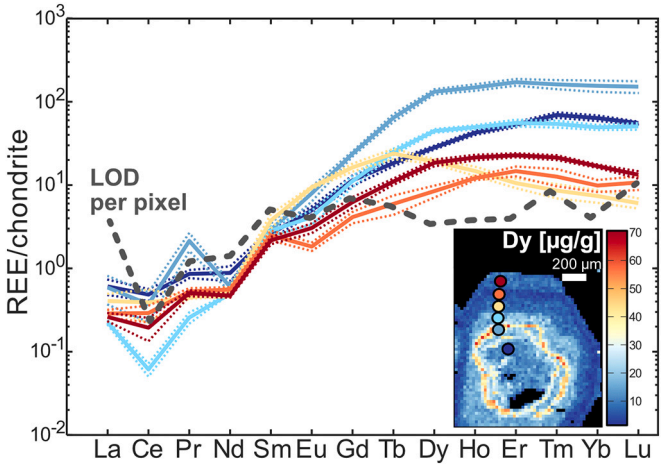

Fig. 14. Chondrite-normalized REE patterns for six circular ROIs from core to rim (blue to red) in the garnet grain of sample DKE-352. The annulus (gray-blue curve) shows enrichment in HREE, while the mantle region (yellow curve) shows enrichment in MREE and depletion in HREE. The rim region again shows a depletion in MREE and enrichment in HREE. Data is extracted using the *Spider* module of XMapTools. The gray dashed line represents the average LOD per pixel for the REE. Colored dashed lines represent the 1 SE of the integrated value of the ROI. Normalization follows Taylor and McLennan (1985). (For interpretation of the references to colour in this figure legend, the reader is referred to the web version of this article.)

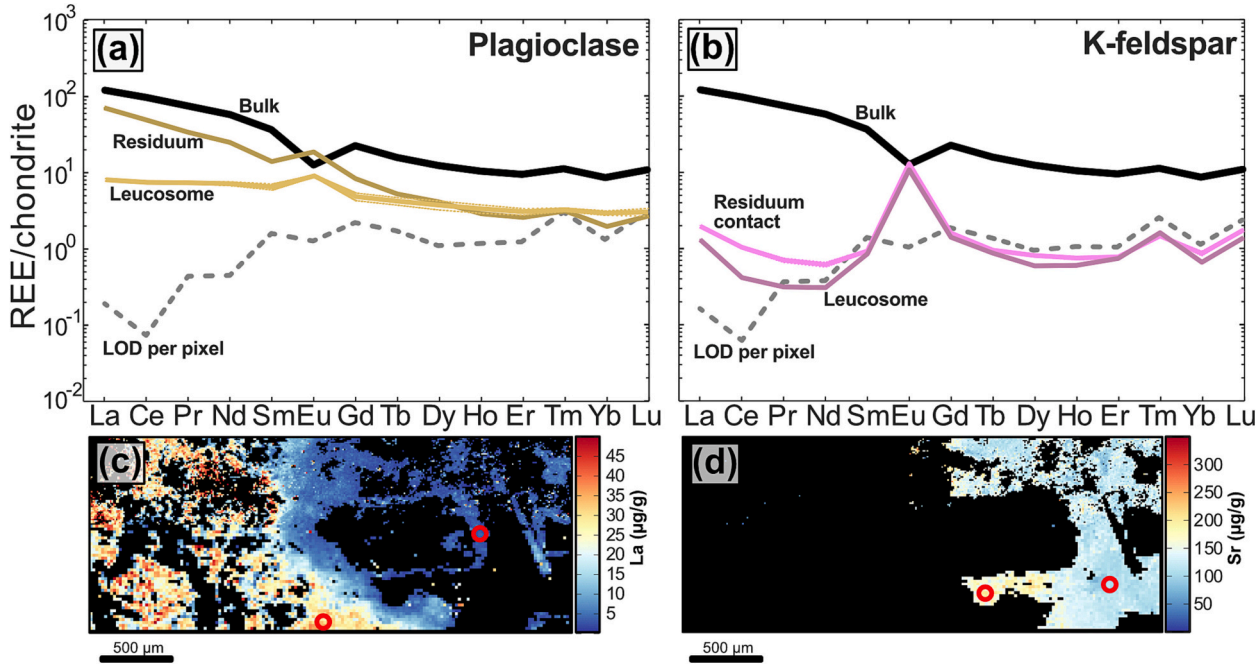

Fig. 15. Chondrite-normalized REE patterns for circular ROIs in sample BA1013. (a) Plagioclase REE patterns from two ROIs, one in the leucosome and one in the residuum. (b) K-feldspar REE patterns from two ROIs, one in the leucosome and one at the contact to the residuum. (c-d) Map of La in plagioclase and Sr in K-feldspar guide the selection of the ROIs (red circles). (a–b) REE pattern of the local bulk composition by integrating biotite, plagioclase and K-feldspar (black solid line). Gray dashed line represents the averaged LOD per pixel of REE in plagioclase and K-feldspar respectively. Normalization follows Taylor and McLennan (1985). (For interpretation of the references to colour in this figure legend, the reader is referred to the web version of this article.)

enrichment in the slow-diffusing elements V, Cr, Ti, and Zr are related to the presence of former minerals which were located in the garnet core prior to garnet growth (Angiboust et al., 2014; Moore et al., 2013; Spandler et al., 2011). Mapping also shows that the core is encircled by an increase in Mn and a sharp increase in the REE content, forming a double annulus. This double annulus is best seen at the highest spatial resolution used for mapping, which is a spot size of 5 µm. The formation of an annulus in garnet, especially in Y + REE, as seen for Dy and Lu (Fig. 6) and Y + HREE (Fig. 14 and supplementary material S2), is often associated with the breakdown of major and/or accessory phases, for example allanite (Boston et al., 2017; Gieré et al., 2011; Pyle and Spear, 2003), but no enrichment in Ca or Sr is detected. The REE pattern also shows an increase in MREE from core to mantle (Fig. 14), which may be related to allanite and/or lawsonite breakdown (Spandler et al., 2003). The rim again shows an increase in HREE and a decrease in MREE, a zonation which is also visible on the major element maps and that can be related to changes in bulk and REE composition. Radial veinlets in X_{sps} are not visible in trace elements, but may be the result of a selective replacement process (Rubatto et al., 2020).

5.2.2. *Migmatite BA1013*

In the migmatitic sample, we demonstrate effective mapping of a large area of two genetically distinct domains (the leucosome, or melt domain, and the residuum) that contain relatively small-scale features. Biotite is enriched in the transition metals Sc, Ti, V, Cr, Mn, Fe, Co, Zn, Zr, and depleted in Li and Rb in the leucosome compared to the residuum (Fig. 10e–h and supplementary material S2). In biotite, patchy zoning is observed for Ba and Cr with comparatively higher contents preserved in the large grain within the leucosome. Interestingly, the transition metals are preserved in peritectic biotite at the melting temperature of 750 °C (Icenhower and London, 1995; Kunz et al., 2022), whereas Li and Rb were mobilized by the melt and enriched in the leucosome (Icenhower and London, 1996). Similarly, Sr contents in plagioclase and K-feldspar show a continuous decrease towards the residuum (Fig. 10a–b). REE maps also show La and Nd enriched sites in plagioclase located in the residuum which correlate with the highest anorthite composition (Fig. 10c–d and Fig. 8). The spatial relationships can be selected for closer examination of REE patterns using ROIs plotted in a chondrite-normalized trace element distribution diagram (Fig. 15). The leucosome domain shows systematic depletion in LREE for plagioclase and K-feldspar compared to the residuum.

5.2.3. *Rutile AS19–3*

The combination of trace element patterns and a thermometer or barometer can allow for linking element behaviour and metamorphic conditions, e.g., the connection between fluid pulses and thermal conditions in subduction zones (Meinhold, 2010). Rutile can provide temperature information from Zr-in-rutile thermometry (Cherniak et al., 2007; Tomkins et al., 2007; Zack et al., 2004) and is able to incorporate a variety of trace elements. Mapping of rutile from sample AS19-3 reveals strong compositional zoning, for example, zoning of Zr in at least five different domains with a range of ~30 µg/g. Temperatures calculated from the Zr-in-rutile thermometer according to eq. 8 in Tomkins et al. (2007) reveal a significant temperature variation of ~40 °C, ranging from 510 to 550 °C (see Fig. 11). To the contrast, a series of single spot analysis could potentially yield a similar temperature range, and most likely would be interpreted to be homogeneous due to the uncertainty of the method. Visualization of the sharp Zr zoning pattern could not be reconstructed by traditional single spot analysis, but can assist in interpreting the formation of the rutile grain. In addition, similar zoning patterns can be observed in other trace elements (e.g., Ta 70 to 180 µg/g, Fig. 11). This might support that zoning domains are the result of multiple growth episodes, as Zr incorporation in rutile is expected to be temperature dependent when the system is in equilibrium and the assemblage is zircon buffered (e.g. Tomkins et al., 2007; Zack et al., 2004). Furthermore, the sharp zoning of trace elements now visible in the maps indicates that diffusion did not play a major role in the post-crystallization history of this rutile grain, as is commonly assumed for grains larger than 200 µm at temperatures of around 500 °C (Cherniak et al., 2007).

6. Conclusions

The detailed comparison between EPMA and LA-ICP-MS data shows that for well calibrated instruments compositional mapping by LA-ICP-MS is robust not only for trace elements but also for major and minor elements. Structural formula and end-member fraction maps can be calculated from LA-ICP-MS data with a quality similar to EPMA mapping. In addition, thermobarometry is more precise than EPMA even when based on major elements (e.g., X_{Mg}) and minor elements (Ti-in-biotite). However, achieving such a high level of accuracy requires calibration over a variable composition for the internal standard element in cases where the phases of interest are chemically variable. In addition, the use of multiple external standards offers the possibility of improving the accuracy of the trace element mass fraction, especially for specific element contents that may not be precisely known in a given external standard material. Moreover, our procedures provide the calculation of LODs for each pixel individually with 95% confidence, thus preventing the interpretation of non-significant data on maps. These novel features are incorporated into the calibration procedure and implemented in XMapTools.

Increasing the spatial resolution by decreasing the spot size results in an improved resolution of geochemical features in relatively small mineral grains, but at the expense of chemical detection power, i.e., increasing LODs as shown on LOD maps. Moreover, while a larger spot size provides better chemical detection power, a low spatial resolution can result in a mixing composition for grains and other chemical features. We also found that directional scanning and lower spatial resolution can lead to a deviation in the true value of a geochemical feature. Using the proposed squared pixel interpolation method and virtual mapping test, we show that the true composition can be resolved when the beam diameter is equal to, or smaller than, the feature size, but may contain a smoothing effect. Finding a way to minimize the smoothing and mixing effect is desirable as it can affect the application of e.g., trace element diffusion modelling in garnet based on quantitative data from maps. The novel procedure described in this paper provides open-source software for improved analysis and calibration of the LA-ICP-MS map, which helps to document major and trace element patterns in solid materials, which in turn may provide new insights into genetic processes.

Code availability

The computer code developed in this study is implemented in the XMapTools software. The code is open source and available via GitHub.

Name: XMapTools
Developer: Pierre Lanari (pierre.lanari@unibe.ch)
Available since: December 2021
Program language: MATLAB
Program size: 27.8 MB
Source code: https://github.com/xmaptools

CRediT authorship contribution statement

Thorsten Andreas Markmann: Conceptualization, Data curation, Formal analysis, Investigation, Methodology, Project administration, Resources, Software, Validation, Visualization, Writing – original draft, Writing – review & editing. **Pierre Lanari:** Conceptualization, Formal analysis, Funding acquisition, Investigation, Methodology, Software, Supervision, Validation, Writing – original draft, Writing – review & editing. **Francesca Piccoli:** Methodology, Resources, Validation. **Thomas Pettke:** Funding acquisition, Methodology, Resources, Validation, Writing – review & editing. **Renée Tamblyn:** Resources, Validation, Writing – review & editing. **Mahyra Tedeschi:** Resources, Writing – review & editing. **Mona Lueder:** Resources, Writing – review & editing. **Barbara E. Kunz:** Methodology, Validation, Writing – review & editing. **Nicolas Riel:** Resources, Writing – review & editing. **Joshua Laughton:** Software, Writing – review & editing.

Declaration of Competing Interest

The authors declare that they have no known competing financial interests or personal relationships that could have appeared to influence the work reported in this paper.

Data availability

The data presented in this study are available in supplementary material (Link) and on Zenodo (https://zenodo.org/doi/10.5281/zenodo.8340229).

Acknowledgments

We thank David Chew and an anonymous reviewer for their detailed reviews, which helped to improve the quality and presentation of the manuscript. We thank Sonja Aulbach for her comments and efficient editorial work. This project has received funding from the European Research Council (ERC) under the European Union's Horizon 2020 research and innovation program (grant 850530), from the Swiss National Science Foundation (SNSF, grants IZSEZ0_210259 and 206021_170722). C. Ganade is thanked for providing sample DKE-352. M. Tedeschi is thankful to the National Council for Scientific and Technological Development (CNPq) for support through productivity grants in scientific research.

Appendix A. Supplementary data

Supplementary data to this article can be found online at https://doi.org/10.1016/j.chemgeo.2023.121895.

References

Ahmed, A.D., Hood, S.B., Cooke, D.R., Belousov, I., 2020. Unsupervised clustering of LA-ICP-MS raster map data for geological interpretation: a case study using epidote from the Yerington district, Nevada. Appl. Comput. Geosci. 8, 100036 https://doi.org/10.1016/j.acags.2020.100036.

Angiboust, S., Pettke, T., De Hoog, J.C.M., Caron, B., Oncken, O., 2014. Channelized fluid flow and eclogite-facies metasomatism along the subduction shear zone. J. Petrol. 55, 883–916. https://doi.org/10.1093/petrology/egu010.

Bissig, T., Hermann, J., 1999. From pre-Alpine extension to Alpine convergence: the example of the southwestern margin of the Margna nappe (Val Malenco, N-Italy). Schweiz. Mineral. Petrogr. Mitt. 79, 363–380.

Boston, K.R., Rubatto, D., Hermann, J., Engi, M., Amelin, Y., 2017. Geochronology of accessory allanite and monazite in the Barrovian metamorphic sequence of the Central Alps, Switzerland. Lithos 286–287, 502–518. https://doi.org/10.1016/j.lithos.2017.06.025.

Bovay, T., Lanari, P., Rubatto, D., Smit, M., Piccoli, F., 2022. Pressure–temperature–time evolution of subducted crust revealed by complex garnet zoning (Theodul Glacier Unit, Switzerland). J. Metam. Geol. 40, 175–206. https://doi.org/10.1111/jmg.12623.

Bussweiler, Y., Gervasoni, F., Rittner, M., Berndt, J., Klemme, S., 2020. Trace element mapping of high-pressure, high-temperature experimental samples with laser ablation ICP time-of-flight mass spectrometry – illuminating melt-rock reactions in the lithospheric mantle. Lithos 352–353, 105282. https://doi.org/10.1016/j.lithos.2019.105282.

Cherniak, D.J., Manchester, J., Watson, E.B., 2007. Zr and Hf diffusion in rutile. Earth Planet. Sci. Lett. 261, 267–279. https://doi.org/10.1016/j.epsl.2007.06.027.

Chew, D., Drost, K., Marsh, J.H., Petrus, J.A., 2021. LA-ICP-MS imaging in the geosciences and its applications to geochronology. Chem. Geol. https://doi.org/10.1016/j.chemgeo.2020.119917.

Drost, K., Chew, D., Petrus, J.A., Scholze, F., Woodhead, J.D., Schneider, J.W., Harper, D.A.T., 2018. An image mapping approach to U-Pb LA-ICP-MS carbonate dating and applications to direct dating of carbonate sedimentation. Geochem. Geophys. Geosyst. 19, 4631–4648. https://doi.org/10.1029/2018GC007850.

Ettre, L.S., 1993. Nomenclature for chromatography (IUPAC recommendations 1993). Pure Appl. Chem. 65, 819–872. https://doi.org/10.1351/pac199365040819.

Fox, M., Tripathy-Lang, A., Shuster, D.L., 2017. Improved spatial resolution of elemental maps through inversion of LA-ICP-MS data. Chem. Geol. 467, 30–41. https://doi.org/10.1016/j.chemgeo.2017.07.001.

Gaidies, F., Morneau, Y.E., Petts, D.C., Jackson, S.E., Zagorevski, A., Ryan, J.J., 2021. Major and trace element mapping of garnet: unravelling the conditions, timing and

rates of metamorphism of the Snowcap assemblage, west-central Yukon. J. Metam. Geol. 39, 133–164. https://doi.org/10.1111/jmg.12562.
Ganade de Araujo, C.E., Weinberg, R.F., Cordani, U.G., 2014. Extruding the Borborema Province (NE-Brazil): a two-stage Neoproterozoic collision process. Terra Nova 26, 157–168. https://doi.org/10.1111/ter.12084.
George, F.R., Gaidies, F., 2017. Characterisation of a garnet population from the Sikkim Himalaya: insights into the rates and mechanisms of porphyroblast crystallisation. Contrib. Mineral. Petrol. 172 https://doi.org/10.1007/s00410-017-1372-y.
George, F.R., Gaidies, F., Boucher, B., 2018. Population-wide garnet growth zoning revealed by LA-ICP-MS mapping: implications for trace element equilibration and syn-kinematic deformation during crystallisation. Contrib. Mineral. Petrol. 173, 1–22. https://doi.org/10.1007/s00410-018-1503-0.
Gieré, R., Rumble, D., Günther, D., Connolly, J., Caddick, M.J., 2011. Correlation of growth and breakdown of major and accessory minerals in metapelites from Campolungo, Central Alps. J. Petrol. 52, 2293–2334. https://doi.org/10.1093/petrology/egr043.
Guillong, M., Meier, D.L., Allan, M.M., Heinrich, C.A., Yardley, B.W.D., 2008. SILLS: a Matlab-based program for the reduction of laser ablation ICP–MS data of homogeneous materials and inclusions. Miner. Assoc. Can. Short Course 40, 328–333.
Gundlach-Graham, A., Günther, D., 2016. Toward faster and higher resolution LA-ICPMS imaging: on the co-evolution of la cell design and ICPMS instrumentation young investigators in analytical and bioanalytical science. Anal. Bioanal. Chem. 408, 2687–2695. https://doi.org/10.1007/s00216-015-9251-8.
Gundlach-Graham, A., Garofalo, P.S., Schwarz, G., Redi, D., Günther, D., 2018. High-resolution, quantitative element imaging of an upper crust, low-angle cataclasite (Zuccale Fault, Northern Apennines) by laser ablation ICP time-of-flight mass spectrometry. Geostand. Geoanal. Res. 42, 559–574. https://doi.org/10.1111/ggr.12233.
Günther, D., Hattendorf, B., 2005. Solid sample analysis using laser ablation inductively coupled plasma mass spectrometry. TrAC Trends Anal. Chem. 24 (3), 255–265. https://doi.org/10.1016/j.trac.2004.11.017.
Hagen-Peter, G., Wang, Y., Hints, O., Prave, A.R., Lepland, A., 2021. Late diagenetic evolution of Ordovician limestones in the Baltoscandian basin revealed through trace-element mapping and in situ U–Pb dating of calcite. Chem. Geol. 585, 120563 https://doi.org/10.1016/j.chemgeo.2021.120563.
Halter, W.E., Pettke, T., Heinrich, C.A., Rothen-Rutishauser, B., 2002. Major to trace element analysis of melt inclusions by laser-ablation ICP-MS: methods of quantification. Chem. Geol. 183, 63–86. https://doi.org/10.1016/S0009-2541(01)00372-2.
Henry, D.J., Guidotti, C.V., Thomson, J.A., 2005. The Ti-saturation surface for low-to-medium pressure metapelitic biotites: implications for geothermometry and Ti-substitution mechanisms. Am. Mineral. 90, 316–328. https://doi.org/10.2138/am.2005.1498.
Icenhower, J., London, D., 1995. An experimental study of element partitioning among biotite, muscovite, and coexisting peraluminous silicic melt at 200 MPa (H2 O). Am. Mineral. 80, 1229–1251. https://doi.org/10.2138/am-1995-11-1213.
Icenhower, J., London, D., 1996. Experimental partitioning of Rb, Cs, Sr, and Ba between alkali feldspar and peraluminous melt. Am. Mineral. 81, 719–734. https://doi.org/10.2138/am-1996-5-619.
Jochum, K.P., Nohl, U., Herwig, K., Lammel, E., Stoll, B., Hofmann, A.W., 2005. GeoReM: a new geochemical database for reference materials and isotopic standards. Geostand. Geoanal. Res. 29, 333–338. https://doi.org/10.1111/j.1751-908x.2005.tb00904.x.
Jollands, M.C., 2020. Assessing analytical convolution effects in diffusion studies: applications to experimental and natural diffusion profiles. PloS One 15, e0241788. https://doi.org/10.1371/journal.pone.0241788.
Konrad-Schmolke, M., Halama, R., Chew, D., Heuzé, C., De Hoog, J., Ditterova, H., 2023. Discrimination of thermodynamic and kinetic contributions to the heavy rare earth element patterns in metamorphic garnet. J. Metam. Geol. 41, 465–490. https://doi.org/10.1111/jmg.12703.
Kunz, B.E., Warren, C.J., Jenner, F.E., Harris, N.B.W., Argles, T.W., 2022. Critical metal enrichment in crustal melts: the role of metamorphic mica. Geology 50, 1219–1223. https://doi.org/10.1130/G50284.1.
Lanari, P., Piccoli, F., 2020. New horizons in quantitative compositional mapping – analytical conditions and data reduction using XMapTools. IOP Conf. Ser. Mater. Sci. Eng. 891, 012016 https://doi.org/10.1088/1757-899X/891/1/012016.
Lanari, P., Vidal, O., De Andrade, V., Dubacq, B., Lewin, E., Grosch, E.G., Schwartz, S., 2014. XMapTools: a MATLAB©-based program for electron microprobe X-ray image processing and geothermobarometry. Comput. Geosci. 62, 227–240. https://doi.org/10.1016/j.cageo.2013.08.010.
Lanari, P., Vho, A., Bovay, T., Airaghi, L., Centrella, S., 2019. Quantitative compositional mapping of mineral phases by electron probe micro-analyser. Geol. Soc. Spec. Publ. 478, 39–63. https://doi.org/10.1144/SP478.4.
Lanari, P., Markmann, T., Laughton, J., Tedeschi, M., 2023. xmaptools/XMapTools_Public: XMapTools 4.2. https://doi.org/10.5281/zenodo.7656957.
Laughton, J., 2023. PTtoolbox. https://doi.org/10.5281/zenodo.10040860.
Longerich, H.P., Jackson, S.E., Günther, D., 1996. Laser ablation inductively coupled plasma mass spectrometric transient signal data acquisition and analyte concentration calculation. J. Anal. At. Spectrom 11, 899–904. https://doi.org/10.1039/JA9961100899.
McCarron, T., Gaidies, F., McFarlane, C.R.M., Easton, R.M., Jones, P., 2014. Coupling thermodynamic modeling and high-resolution in situ LA-ICP-MS monazite geochronology: evidence for Barrovian metamorphism late in the Grenvillian history of southeastern Ontario. Mineral. Petrol. 108, 741–758. https://doi.org/10.1007/s00710-014-0343-5.
Meinhold, G., 2010. Rutile and its applications in earth sciences. Earth Sci. Rev. 102, 1–28. https://doi.org/10.1016/j.earscirev.2010.06.001.
Moore, S.J., Carlson, W.D., Hesse, M.A., 2013. Origins of yttrium and rare earth element distributions in metamorphic garnet. J. Metam. Geol. 31, 663–689. https://doi.org/10.1111/jmg.12039.
Norris, C.A., Danyushevsky, L., Olin, P., West, N.R., 2021. Elimination of aliasing in LA-ICP-MS by alignment of laser and mass spectrometer. J. Anal. At. Spectrom 36, 733–739. https://doi.org/10.1039/d0ja00488j.
Paton, C., Hellstrom, J., Paul, B., Woodhead, J., Hergt, J., 2011. Iolite: freeware for the visualisation and processing of mass spectrometric data. J. Anal. At. Spectrom 26, 2508–2518. https://doi.org/10.1039/c1ja10172b.
Paul, B., Paton, C., Norris, A., Woodhead, J., Hellstrom, J., Hergt, J., Greig, A., 2012. CellSpace: a module for creating spatially registered laser ablation images within the Iolite freeware environment. J. Anal. At. Spectrom 27, 700. https://doi.org/10.1039/c2ja10383d.
Paul, B., Woodhead, J.D., Paton, C., Hergt, J.M., Hellstrom, J., Norris, C.A., 2014. Towards a method for quantitative LA-ICP-MS imaging of multi-phase assemblages: mineral identification and analysis correction procedures. Geostand. Geoanal. Res. 38, 253–263. https://doi.org/10.1111/j.1751-908X.2014.00270.x.
Petrus, J.A., Chew, D.M., Leybourne, M.I., Kamber, B.S., 2017. A new approach to laser-ablation inductively-coupled-plasma mass-spectrometry (LA-ICP-MS) using the flexible map interrogation tool 'Monocle.'. Chem. Geol. 463, 76–93. https://doi.org/10.1016/j.chemgeo.2017.04.027.
Pettke, T., Heinrich, C.A., Ciocan, A.C., Günther, D., 2000. Quadrupole mass spectrometry and optical emission spectroscopy: detection capabilities and representative sampling of short transient signals from laser-ablation. J. Anal. At. Spectrom 15, 1149–1155. https://doi.org/10.1039/B001910K.
Pettke, T., Oberli, F., Audétat, A., Guillong, M., Simon, A.C., Hanley, J.J., Klemm, L.M., 2012. Recent developments in element concentration and isotope ratio analysis of individual fluid inclusions by laser ablation single and multiple collector ICP-MS. Ore Geol. Rev. 44, 10–38. https://doi.org/10.1016/j.oregeorev.2011.11.001.
Phillips, S.E., Argles, T.W., Warren, C.J., Harris, N.B.W., Kunz, B.E., 2023. Kyanite petrogenesis in migmatites: resolving melting and metamorphic signatures. Contrib. Mineral. Petrol. 178, 10. https://doi.org/10.1007/s00410-022-01991-w.
Piccoli, F., Lanari, P., Hermann, J., Pettke, T., 2022. Deep subduction, melting, and fast cooling of metapelites from the Cima Lunga Unit, Central Alps. J. Metam. Geol. 40, 121–143. https://doi.org/10.1111/jmg.12621.
Plotnikov, A., Vogt, C., Wetzig, K., Kyriakopoulos, A., 2008. A theoretical approach to the interpretation of the transient data in scanning laser ablation inductively coupled plasma mass spectrometry: Consideration of the geometry of the scanning area. Spectrochim. Acta Part B Atom. Spectrosc. 63, 474–483. https://doi.org/10.1016/j.sab.2007.12.012.
Pyle, J.M., Spear, F.S., 2003. Yttrium zoning in garnet: coupling of major and accessory phases during metamorphic reactions. Am. Mineral. 88, 708.
Raimondo, T., Payne, J., Wade, B., Lanari, P., Clark, C., Hand, M., 2017. Trace element mapping by LA-ICP-MS: assessing geochemical mobility in garnet. Contrib. Mineral. Petrol. 172, 17. https://doi.org/10.1007/s00410-017-1339-z.
Riel, N., Guillot, S., Jaillard, E., Martelat, J.E., Paquette, J.L., Schwartz, S., Goncalves, P., Duclaux, G., Thebaud, N., Lanari, P., Janots, E., Yuquilema, J., 2013. Metamorphic and geochronogical study of the Triassic El Oro metamorphic complex, Ecuador: implications for high-temperature metamorphism in a forearc zone. Lithos 156–159, 41–68. https://doi.org/10.1016/j.lithos.2012.10.005.
Rittner, M., Müller, W., 2012. 2D mapping of LA-ICPMS trace element distributions using R. Comput. Geosci. 42, 152–161. https://doi.org/10.1016/j.cageo.2011.07.016.
Rubatto, D., Burger, M., Lanari, P., Hattendorf, B., Schwarz, G., Neff, C., Keresztes Schmidt, P., Hermann, J., Vho, A., Günther, D., 2020. Identification of growth mechanisms in metamorphic garnet by high-resolution trace element mapping with LA-ICP-TOFMS. Contrib. Mineral. Petrol. 175, 61. https://doi.org/10.1007/s00410-020-01700-5.
Savard, D., Dare, S., Bédard, L.P., Barnes, S., 2023. A new mapping protocol for laser ablation (with fast-funnel) coupled to a time-of-flight mass spectrometer (LA-FF-ICP-ToF-MS) for the rapid, simultaneous quantification of multiple minerals. Geostand. Geoanal. Res. 1–23 https://doi.org/10.1111/ggr.12482.
Spandler, C., Hermann, J., Arculus, R., Mavrogenes, J., 2003. Redistribution of trace elements during prograde metamorphism from lawsonite blueschist to eclogite facies; implications for deep subduction-zone processes. Contrib. Mineral. Petrol. 146, 205–222. https://doi.org/10.1007/s00410-003-0495-5.
Spandler, C., Pettke, T., Rubatto, D., 2011. Internal and external fluid sources for eclogite-facies veins in the Monviso Meta-ophiolite, Western Alps: implications for fluid flow in subduction zones. J. Petrol. 52, 1207–1236. https://doi.org/10.1093/petrology/egr025.
Tamblyn, R., Hand, M., Kelsey, D., Anczkiewicz, R., Och, D., 2020. Subduction and accumulation of lawsonite eclogite and garnet blueschist in eastern Australia. J. Metam. Geol. 38, 157–182. https://doi.org/10.1111/jmg.12516.
Tamblyn, R., Brown, D., Hand, M., Morrissey, L., Clark, C., Anczkiewicz, R., 2021. The 2 Ga eclogites of Central Tanzania: directly linking age and metamorphism. Lithos 380–381, 105890. https://doi.org/10.1016/j.lithos.2020.105890.
Taylor, S.R., McLennan, S.M., 1985. The Continental Crust: Its Composition and Evolution. Blackwell, Oxford.
Tomkins, H.S., Powell, R., Ellis, D.J., 2007. The pressure dependence of the zirconium-in-rutile thermometer. J. Metam. Geol. 25, 703–713. https://doi.org/10.1111/j.1525-1314.2007.00724.x.
Tracy, R.J., 1982. Chapter 9. Compositional zoning and inclusions in metamorphic minerals. In: Characterization of Metamorphism through Mineral Equilibria. De Gruyter, pp. 354–398. https://doi.org/10.1515/9781501508172-013.

Tual, L., Smit, M.A., Cutts, J., Kooijman, E., Kielman-Schmitt, M., Majka, J., Foulds, I., 2022. Rapid, paced metamorphism of blueschists (Syros, Greece) from laser-based zoned Lu-Hf garnet chronology and LA-ICPMS trace element mapping. Chem. Geol. 607, 121003 https://doi.org/10.1016/j.chemgeo.2022.121003.

Ubide, T., McKenna, C.A., Chew, D.M., Kamber, B.S., 2015. High-resolution LA-ICP-MS trace element mapping of igneous minerals: in search of magma histories. Chem. Geol. 409, 157–168. https://doi.org/10.1016/j.chemgeo.2015.05.020.

Ulrich, T., Kamber, B.S., Jugo, P.J., Tinkham, D.K., 2009. Imaging element- distribution patterns in minerals by Laser Ablation–Inductively Coupled Plasma–Mass Spectrometry (LA–ICP–MS). Can. Mineral. 47, 1001–1012. https://doi.org/10.3749/canmin.47.5.1001.

van Elteren, J.T., Šelih, V.S., Šala, M., 2019. Insights into the selection of 2D LA-ICP-MS (multi)elemental mapping conditions. J. Anal. At. Spectrom 34, 1919–1931. https://doi.org/10.1039/C9JA00166B.

van Elteren, J.T., Šala, M., Metarapi, D., 2021. Comparison of single pulse, multiple dosage, and 2D oversampling / deconvolution LA-ICPMS strategies for mapping of (ultra)low-concentration samples. Talanta 235, 122785. https://doi.org/10.1016/j.talanta.2021.122785.

Van Malderen, van Elteren, Šelih, V.S., Vanhaecke, F., 2018. Considerations on data acquisition in laser ablation-inductively coupled plasma-mass spectrometry with low-dispersion interfaces. Spectrochimica Acta - Part B Atomic Spectroscopy 140, 29–34. https://doi.org/10.1016/j.sab.2017.11.007.

Van Malderen, S.J.M., Van Elteren, J.T., Vanhaecke, F., 2015. Development of a fast laser ablation-inductively coupled plasma-mass spectrometry cell for sub-μm scanning of layered materials. J. Anal. At. Spectrom 30, 119–125. https://doi.org/10.1039/c4ja00137k.

Vielzeuf, D., Holloway, J.R., 1988. Experimental determination of the fluid-absent melting relations in the pelitic system. Contrib. Mineral. Petrol. 98, 257–276. https://doi.org/10.1007/BF00375178.

Warr, L.N., 2021. IMA–CNMNC approved mineral symbols. Mineral. Mag. 85, 291–320. https://doi.org/10.1180/mgm.2021.43.

Woodhead, J.D., Hellstrom, J., Hergt, J.M., Greig, A., Maas, R., 2007. Isotopic and elemental imaging of geological materials by laser ablation inductively coupled plasma-mass spectrometry. Geostand. Geoanal. Res. 31 https://doi.org/10.1111/j.1751-908X.2007.00104.x, 071117031212003.

Woodhead, J., Hellstrom, J., Paton, C., Hergt, J., Greig, A., Maas, R., 2008. A guide to depth profiling and imaging applications of ICP-MS. Miner. Assoc. Can. Short Course Series 135–145.

Woodhead, J.D., Horstwood, M.S.A., Cottle, J.M., 2016. Advances in isotope ratio determination by LA-ICP-MS. Elements 12, 317–322. https://doi.org/10.2113/gselements.12.5.317.

Zack, T., Moraes, R., Kronz, A., 2004. Temperature dependence of Zr in rutile: empirical calibration of a rutile thermometer. Contrib. Mineral. Petrol. 148, 471–488. https://doi.org/10.1007/s00410-004-0617-8.

Zhu, Z.-Y., Cook, N., Yang, T., Ciobanu, C., Zhao, K.-D., Jiang, S.-Y., 2016. Mapping of sulfur isotopes and trace elements in sulfides by LA-(MC)-ICP-MS: potential analytical problems, improvements and implications. Minerals 6, 110. https://doi.org/10.3390/min6040110.